

Following is the Accepted Version of the article

Marko Nagode, Jernej Klemenc, Simon Oman, Domen Šeruga (2021)

A closed-form solution for temperature-dependent elastoplastic problems using the Prandtl operator approach

published by

Communications in Nonlinear Science and Numerical Simulation.

The formal publication can be accessed at

<https://doi.org/10.1016/j.cnsns.2021.105839>

This version of the article may be used for non-commercial purposes in accordance with Elsevier's Green open access policy (CC-BY-NC-ND license).

A closed-form solution for temperature-dependent elastoplastic problems using the Prandtl operator approach

Marko Nagode, Jernej Klemenc, Simon Oman, Domen Šeruga*

University of Ljubljana, Faculty of Mechanical Engineering, Ljubljana, Slovenia

Abstract

Finite element simulations of the temperature-dependent stress-strain response in the elastoplastic region of a material usually involve incremental procedures based on the Newton–Raphson iterative scheme. Although essential to obtaining the correct result, iterations inherently extend the computational time of the simulations. In order to increase the computational effectiveness of such finite element simulations, a novel solution technique is presented here, which introduces a closed-form determination of the elastoplastic stress-strain response using the Prandtl operator approach. Using this solution, the iterative procedure is no longer required. The positions of the tensile-compressive and shear meridians of the Haigh–Westergaard coordinate space are first conveniently modified, which then enables the configuration of coordinate-independent play operators. These play operators connect the stress and the strain tensors in a unique closed-form solution that significantly increases the computational power of the simulations, while retaining both the vigorous stability of the procedure and the high accuracy of the results. The method is successfully validated on several load cases, consisting of variable tensile, shear and combined thermomechanical load histories. Limitations of the current version of the approach, that are a part of on-going research, include extremely low values of the third deviatoric strain-invariant increments, in which the directions of movement of the yield surfaces can be changed. Furthermore, the discretisation of the cyclic stress-strain curves plays an important role. The optimal positions of the yield strains are hence another important issue for future studies. Additionally, the consistent material Jacobian results in an unsymmetric form in e.g. Abaqus when engineering shear strains are provided in the simulations and thus the computational

power is not fully used. Nevertheless, the results using the Prandtl operator approach, when compared to the results obtained using the conventional, Besseling material model, show excellent agreement, while substantially reducing the computational time by up to 45 %.

Keywords:

Prandtl operators, finite element method, thermomechanical loading, plasticity, uniaxial, fatigue

1. Introduction

During periods of operation, the materials used for the structural components of power plants, exhaust systems or pressure vessels and piping undergo a wide range of strains and temperatures [1–8]. Variable, cyclic thermomechanical loads cause load-history-dependent, stress-strain responses in the materials of such components. Simulations of the responses in a virtual environment are of great significance for the engineers and researchers who design and optimise new structural components [9–12]. Accurate simulations and high computational speeds enable the reliable predictions of the material behaviour and permit additional design iterations during the constantly reducing, assessed time windows in the R&D process [13, 14].

For ductile isotropic materials such as some commonly used metals, e.g. alloy steels and aluminium alloys, it is accepted that a material under load will yield when the yield surface of a general stress state at an observed location on a structural component $F = F(\sigma_{ij})$ equals zero, regardless of the coordinate system used for the observation [15, 16]. Furthermore, the dependence of the general stress state can be expressed either in terms of the principal values $F(\sigma_{ij}) = F(\sigma_1, \sigma_2, \sigma_3)$ or in terms of the invariants $F(\sigma_{ij}) = F(I_1, J_2, \cos 3\Theta)$. The advantage of the latter formulation is the separate representation of the hydrostatic stress contained in the first stress invariant I_1 , and the shape distortion of the material, incorporated into both the second deviatoric stress invariant J_2 and the Lode angle Θ [15–20]. Moreover, such a formulation of the yield surface also allows for a graphically expressive

*Corresponding author. E-mail: domen.seruga@fs.uni-lj.si, Tel.: +386-1-4771-743, Fax: +386-1-4214-074
Preprint submitted to Communications in Nonlinear Science & Numerical Simulation *January 14, 2021*

representation of the stress-strain states in the well-known Haigh–Westergaard coordinate system. Three important meridians emerge in the Haigh–Westergaard coordinate space, depending on the type of loading. The tensile meridian refers to the uniaxial tensile stresses and the biaxial compressive stresses. The compressive meridian specifies the position of the uniaxial compressive stress conditions, whereas the shear meridian corresponds to the pure shear-stress states [15, 21]. The meridians are positioned in the Haigh–Westergaard coordinate space by the Lode angle at 0 , 30 and 60° (as shown in Fig. 1a).

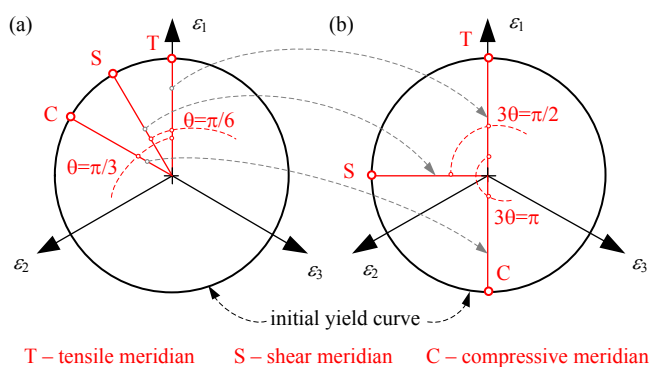


Figure 1: a) Conventional Haigh–Westergaard coordinate system and b) modified Haigh–Westergaard coordinate system.

Beyond the yield point, plastic strains develop in the material, depending on both the thermal and the mechanical load histories of the structural component. Consequently, the yield surface also changes its size, shape and position with the development of these plastic strains [15, 19, 20, 22]. In mechanics, various models exist to describe this change, also referred to as the hardening rule. Initial proposals about isotropic hardening by Hill [23] and kinematic hardening by Melan [24] and Prager [25] have since been developed into various alternatives. Some recent developments have investigated material models based on internal state variable theories that can be used to predict the behaviour of materials under monotonic or cyclic loadings at constant or varying temperatures [9, 26–29]. Lee et al. [26] proposed a temperature-dependent constitutive model using a continuum-based distortional hardening law, which affects the shape of the yield surface depending on the loading direction. Qi et al. [27] developed a nonlinear elastic-viscoplastic constitutive model based on

a parallel rheological framework. Xie et al. [9] presented a damage-coupled cyclic elastic-viscoplastic constitutive model involving the strain-range, strain-rate and loading histories' dependence to predict the complex cyclic behaviours of the material at elevated temperatures. Xing et al. [28] explored simulations of the proportional and non-proportional cyclic deformation of 316L stainless steel at room temperature. A cyclic plasticity model for a strain-induced martensite phase transformation was established by correlating the isotropic hardening and the kinetics of the martensitic transformation by Luo et al. [29]. A simplified plasticity model by Madrigal et al. [30] for multiaxial, non-proportional cyclic loading enables simulations of the biaxial plane stress state along non-proportional paths. Recent studies also report on the development of crystal plasticity models that consider the underlying physical micro-mechanisms to simulate the behaviour of the material under cyclic thermomechanical operating conditions [31–34]. Petkov et al. [31] examined the predictive capabilities of a crystal plasticity model for inelastic deformation that captures the evolution of the dislocation structure, precipitates and solute atom distributions on the microscale. Rodas et al. [32] proposed a model capable of representing the interactions in single-crystal superalloys for three-dimensional components by considering kinematic hardening to account for the Bauschinger effect during load reversals, changes in the strain rate during cyclic loading excursions and the evolution of dislocations. The modelling strategy of Cruzado et al. [33] was based on the computational homogenisation of a volume element of the microstructure, which included information about the grain size, shape and orientation distributions. Farooq et al. [34] recently characterised the cyclic response of face-centred-cubic polycrystalline materials on both the macroscopic and local levels using rate-independent crystal plasticity with kinematic hardening. However, considerable attention must be paid to the determination of the model parameters with the crystal plasticity models. While consideration of isotropic hardening is important during the initial stabilisation of the stress-strain response of a material, kinematic hardening is more pronounced during the cyclic loading of mechanical components during the entire lifetime [9, 15, 35, 36]. Kinematic hardening includes a description of the Bauschinger effect using the Masing rule and the memory rules that define the behaviour of the nested hysteresis loops during variable load histories [11, 16, 35].

A classic implicit approach to the simulation of elastoplasticity at the material point level using the finite element method (FEM) involves return methods consisting of a predictor–corrector routine that is then followed by a Newton–Raphson iteration scheme in order to determine the correct plastic strain [9, 12, 15, 26, 29, 37–39]. This approach ensures stable and accurate problem-solving, but results in a rather elaborate solution strategy, which consequently also extends the computational time. Clearly, the Newton–Raphson iteration scheme in multiple dimensions ensures a rapid rate of convergence when the solution is near the searching point. However, the number of iterations might increase if the solution extends away from the searching point, i.e. if a considerable load increase is applied to the analysed material [40]. Furthermore, an incorrect approach might not only lead to an incorrect stress solution for the given strain increment, but can also delay the convergence of the iteration procedure or can even start diverging in the search for the solution [16].

The motivation for the method presented in this paper was the increase of the computational power of the elastoplastic stress-strain simulation using FEM, while maintaining both the stability and accuracy of the calculation. The novelty of the method is the introduction of a closed-form determination of the elastoplastic stress-strain states without the utilisation of either the predictor–corrector routine or the Newton–Raphson iterative scheme, which presumably extend the computational time due to the repetitious procedure. Instead, an elastoplastic stress-strain solution for variable thermomechanical loads has been formulated so as to allow a direct solution to the problem. This required establishing of modified meridians of the Haigh–Westergaard coordinate space (Fig. 1b) and the utilisation of the Prandtl operator approach. The Prandtl operator approach has already been successfully implemented into the FEM as a part of the predictor–corrector routine [11], which already enabled a reduction of the computational time during the elastoplastic structural analyses of thermomechanically loaded components. Here, we extend the use of the Prandtl operator approach to such a level that the predictor–corrector routine becomes superfluous. The exact stress-tensor solution is obtained directly for a given strain tensor. This step additionally improves the computational power of the simulations and hence further reduces the computational time. The method is especially applicable to the cyclic

temperature-dependent structural analyses of complex mechanical structures composed of a large number of finite elements where a reduction of the computational time is most welcome. Nevertheless, the method without any modifications is also applicable to monotonic loads. It is the user’s responsibility however to provide the suitable material parameters which correspond to either the tensile stress-strain relationship or the stabilised cyclic stress-strain conditions which have been used for the ferritic stainless steel EN 1.4512 in this study. Supplementary literature on the development of the Prandtl operator approach can be found in [41–47] and applications of the approach to various mechanical components subjected to variable thermomechanical loadings are provided in [6, 48–52]. The new approach can be applied to simulate the stress-strain response of monotonically or cyclically loaded solids with temperature-dependent isotropic elastoplastic material properties and multilinear kinematic hardening. As the yield criterion is independent from the hydrostatic stress, the approach can be applied to simulate the behaviour of ductile isotropic materials, such as some metals, during operation, e.g. structural components of power plants, exhaust systems or pressure vessels and piping.

The method is first presented for a general solution step, given the converged solution from a previous simulation step. Next, the determination of the material parameters is presented, followed by a calculation of the consistent material Jacobian. Numerical examples provide the working principle of the method and allow a comparison of the results with a classic model for cyclic elastoplastic solutions with multilinear kinematic hardening, i.e. the Besseling model [53]. We refer to the *method using the Prandtl operator approach* also using the expression *Prandtl model* from here on, which is more convenient especially when comparisons with the Besseling model are being drawn.

2. Method

2.1. Direct solution of the cyclic elastoplasticity with multilinear kinematic hardening

It is assumed that the stress tensor $\sigma_{ij}^{(1)}$ and the strain tensor $\varepsilon_{ij}^{(1)}$ for the last accepted equilibrium state (1), including the strain-tensor increment $\Delta\varepsilon_{ij}$, are known. Small deformations are assumed. The strain tensor in the current state (2) can thus be calculated as

$$\varepsilon_{ij}^{(2)} = \varepsilon_{ij}^{(1)} + \Delta\varepsilon_{ij}. \quad (1)$$

Now the aim is to develop an exact closed-form expression for the stress tensor in the current state (2) as

$$\sigma_{ij}^{(2)} = \sigma_{ij}^{(1)} + \Delta\sigma_{ij}, \quad (2)$$

which at any point during its determination will not involve an iterative numerical routine. If the effective stress σ_{eff} , as a scalar equivalent of the stress tensor [15], is an arbitrary, monotonically increasing function of the effective strain ε_{eff} attained at an arbitrary, but constant, temperature T , we will show that no iteration is required to solve Eq. 2 if the hardening law $\sigma_{\text{eff}} = f(\varepsilon_{\text{eff}})$ is approximated by $n_q - 1$ linear segments encapsulated into a form of radial Prandtl operators. The main steps of the procedure are also given in Fig. 2 to support the comprehension of the solution.

The procedure for determining $\Delta\sigma_{ij}$ and, consequently $\sigma_{ij}^{(2)}$ in Eq. 2 begins with the initialisation of the variables used during the calculation. Presumably, there is initially no residual strain, so the normal, shear and radial back-strains in the deviatoric plane are introduced as

$$E_{nl}^{(1)} = E_{sl}^{(1)} = E_{\rho l}^{(1)} = 0, \quad l = 1, \dots, n_q, \quad (3)$$

the normal, shear, radial and maximum strains in the deviatoric plane are initialised as

$$e_n^{(1)} = e_s^{(1)} = e_\rho^{(1)} = e_{\text{max}}^{(1)} = 0 \quad (4)$$

and the normal, shear and radial stresses in the deviatoric plane are set as

$$s_n^{(1)} = s_s^{(1)} = s_\rho^{(1)} = 0. \quad (5)$$

The l -th radial back-strain can be graphically explained as the radial coordinates of the centre E_l for the l -th yield function with the radius q_l in the deviatoric plane (Fig. 3a). The first radial back-strain denoted by the point P is thus the coordinate of the centre E_1 of the first yield function with the radius $q_1 = 0$. If the point P is located along the space diagonal of the principal axes ε_1 , ε_2 and ε_3 , then all the principal strains in Fig. 3a are

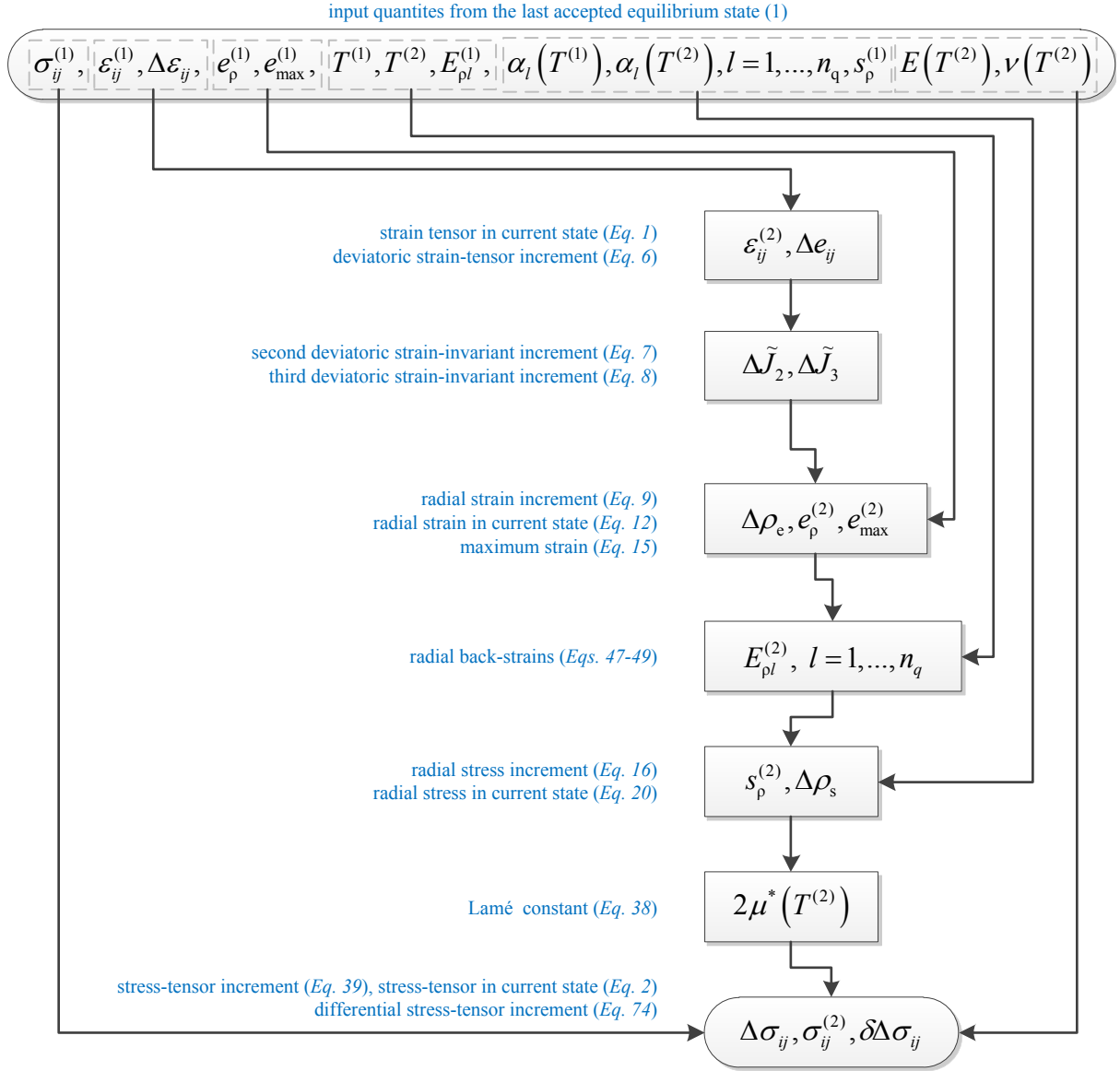


Figure 2: Main steps of the direct solution of the cyclic elastoplasticity with multilinear kinematic hardening.

equal, the space diagonal going through the point N is the hydrostatic axis and the distance $|NP| = \rho_e = 0$. Otherwise, the distance $|NP|$ in Fig. 3b of the point P to the hydrostatic axis is greater than zero.

Finally, $3\theta_e$ is the angle in the deviatoric plane between the projection of the ε_1 axis onto the deviatoric plane and the line NP . The angle θ_e is the Lode angle [15–17]. A modified

and the third deviatoric strain-invariant increment is calculated as

$$\Delta\tilde{J}_3 = \frac{1}{3}\Delta e_{ij}\Delta e_{jk}\Delta e_{ki}. \quad (8)$$

The radial strain increment can be expressed by considering the relations in the deviatoric plane [15] as

$$\Delta\rho_e = \sqrt{2\Delta\tilde{J}_2}. \quad (9)$$

The normal strain increment in the deviatoric plane Δe_n can hence be determined as

$$\Delta e_n = \frac{3\sqrt{6}\Delta\tilde{J}_3}{\Delta\rho_e^2} \quad (10)$$

and the shear strain increment in the deviatoric plane can be determined as

$$\Delta e_s = \sqrt{\Delta\rho_e^2 - \Delta e_n^2}. \quad (11)$$

If $\Delta\tilde{J}_3 \geq 0$, both the radial and the normal strain increments are positive; if $\Delta\tilde{J}_3 < 0$, they are negative. Conventionally, the sign of the shear strain increment equals the sign of the normal strain increment. As the model is driven by the radial movement of the yield functions, only the movement and the sign of the radial strain increment are essential. Furthermore, the radial strain in the deviatoric plane for the current state is then calculated as

$$e_\rho^{(2)} = e_\rho^{(1)} + \Delta\rho_e. \quad (12)$$

The normal and shear strains in the vertical and horizontal directions of the modified Haigh–Westergaard coordinate system, respectively, can be worked out as

$$e_n^{(2)} = e_n^{(1)} + \Delta e_n \quad (13)$$

and

$$e_s^{(2)} = e_s^{(1)} + \Delta e_s. \quad (14)$$

To increase the computational power of the algorithm, the maximum strain in the deviatoric plane is calculated as

$$e_{\max}^{(2)} = \max(e_{\max}^{(1)}, e_\rho^{(2)}). \quad (15)$$

Next, the radial back-strains $E_{\rho l}^{(2)}$ and the radial back-strain increments $\Delta\rho_{el}$ are calculated as explained in Section 2.2. Afterwards, the radial stress in the deviatoric plane for the current state is calculated as

$$s_{\rho}^{(2)} = \sum_{l=1}^{n_q} \alpha_l(T^{(2)}) E_{\rho l}^{(2)} \quad (16)$$

or equivalently as

$$s_{\rho}^{(2)} = \sum_{l=1}^{n_q} \alpha_l(T^{(2)}) \Delta\rho_{el} + \sum_{l=1}^{n_q} \alpha_l(T^{(2)}) E_{\rho l}^{(1)}. \quad (17)$$

The details of the calculation of the Prandtl densities $\alpha_l(T^{(2)})$ are given in Section 2.3.

Eq. 17 can be subsequently rewritten as

$$s_{\rho}^{(2)} = \sum_{l=1}^{n_q} \alpha_l(T^{(2)}) \Delta\rho_{el} + \sum_{l=1}^{n_q} \alpha_l(T^{(1)}) E_{\rho l}^{(1)} + \sum_{l=1}^{n_q} (\alpha_l(T^{(2)}) - \alpha_l(T^{(1)})) E_{\rho l}^{(1)}. \quad (18)$$

Since $s_{\rho}^{(1)} = \sum_{l=1}^{n_q} \alpha_l(T^{(1)}) E_{\rho l}^{(1)}$ and $\Delta\alpha_l = \alpha_l(T^{(2)}) - \alpha_l(T^{(1)})$, the radial stress in the deviatoric plane for the current state is given by

$$s_{\rho}^{(2)} = \sum_{l=1}^{n_q} \alpha_l(T^{(2)}) \Delta\rho_{el} + s_{\rho}^{(1)} + \sum_{l=1}^{n_q} \Delta\alpha_l E_{\rho l}^{(1)}. \quad (19)$$

The corresponding radial stress increment in the deviatoric plane is then

$$\Delta\rho_s = s_{\rho}^{(2)} - s_{\rho}^{(1)}, \quad (20)$$

or equivalently,

$$\Delta\rho_s = \sum_{l=1}^{n_q} \alpha_l(T^{(2)}) \Delta\rho_{el} + \sum_{l=1}^{n_q} \Delta\alpha_l E_{\rho l}^{(1)} = \Delta\rho_s^{(M)} + \Delta\rho_s^{(T)}. \quad (21)$$

A single radial stress increment $\Delta\rho_{sl}$ is hence a consequence of the mechanical contribution $\Delta\rho_{sl}^{(M)}$ and the thermal contribution $\Delta\rho_{sl}^{(T)}$. Most importantly, all the radial stress increments appear in the same direction, as depicted in Fig. 4.

From Fig. 5 it follows that when the point P moves from the last accepted equilibrium state (1) to the current state (2), it is supposed that all the centres of the yield functions either move in the same direction or are at rest. The angle $3\Delta\theta_e$ can thus be calculated as

$$\tan 3\Delta\theta_e = \frac{\Delta e_s}{\Delta e_n}. \quad (22)$$

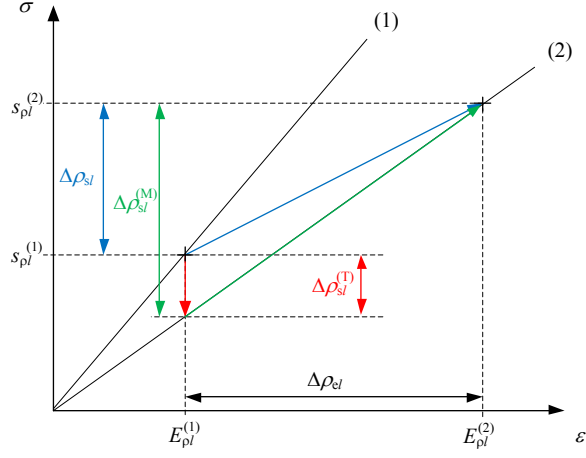


Figure 4: Equal orientation of the total, mechanical and thermal stress increments during the transition from the last accepted equilibrium state (1) to the current state (2).

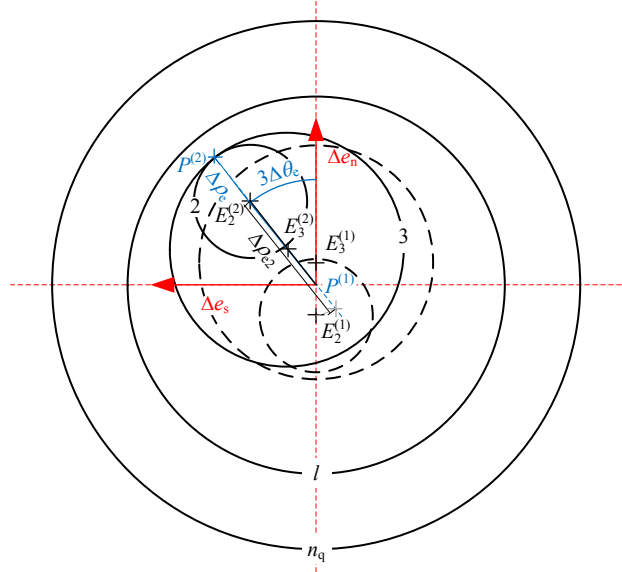


Figure 5: Modified Haigh–Westergaard coordinate system. Transition from the last accepted equilibrium state (1) to the current state (2).

Furthermore, if the back-strain increments $\Delta E_{nl} = E_{nl}^{(2)} - E_{nl}^{(1)}$ and $\Delta E_{sl} = E_{sl}^{(2)} - E_{sl}^{(1)}$ are observed, the angle $3\Delta\theta_e$ can also be expressed as

$$\tan 3\Delta\theta_e = \frac{\Delta E_{sl}}{\Delta E_{nl}}, \quad (23)$$

where the back-strain increments are calculated as

$$\Delta E_{nl} = \Delta \rho_{el} \cos 3\Delta\theta_e \quad (24)$$

and

$$\Delta E_{sl} = \Delta \rho_{el} \sin 3\Delta\theta_e. \quad (25)$$

Following the relations in the deviatoric plane [15], the first principal deviatoric strain increment can be obtained as

$$\Delta e_1 = \sqrt{\frac{2}{3}} \Delta \rho_e \cos \Delta\theta_e \quad (26)$$

and similarly [15], the first principal deviatoric stress increment can be expressed as

$$\Delta s_1 = \sqrt{\frac{2}{3}} \Delta \rho_s \cos \Delta\theta_s. \quad (27)$$

In Eq. 27, the angle $3\Delta\theta_s$ can be calculated as

$$\tan 3\Delta\theta_s = \frac{\Delta s_s}{\Delta s_n}, \quad (28)$$

where the normal and shear stress increments in the deviatoric plane Δs_n and Δs_s are connected to the angle $3\Delta\theta_s$ and the radial stress increment in the deviatoric plane $\Delta \rho_s$ as

$$\Delta s_n = \Delta \rho_s \cos 3\Delta\theta_s \quad (29)$$

and

$$\Delta s_s = \Delta \rho_s \sin 3\Delta\theta_s. \quad (30)$$

Inserting Eq. 21 into Eqs. 29 and 30, the separation of the normal and shear stress increments is observed as

$$\Delta s_n = \Delta \rho_s^{(M)} \cos 3\Delta\theta_s + \Delta \rho_s^{(T)} \cos 3\Delta\theta_s = \Delta s_n^{(M)} + \Delta s_n^{(T)} \quad (31)$$

and

$$\Delta s_s = \Delta \rho_s^{(M)} \sin 3\Delta\theta_s + \Delta \rho_s^{(T)} \sin 3\Delta\theta_s = \Delta s_s^{(M)} + \Delta s_s^{(T)}. \quad (32)$$

Recalling the parallel occurrence of the total, mechanical and thermal stress increments (Fig. 4) and considering the relation between the back-strain increments ΔE_{nl} and ΔE_{sl}

with the strain increment $\Delta\rho_{el}$ according to Eqs. 24 and 25, the equivalence of the angles $3\Delta\theta_e$ and $3\Delta\theta_s$ can be calculated as

$$\tan 3\Delta\theta_s = \frac{\Delta s_s}{\Delta s_n} = \frac{\Delta s_s^{(M)}}{\Delta s_n^{(M)}} = \frac{\Delta s_s^{(T)}}{\Delta s_n^{(T)}} = \tan 3\Delta\theta_e. \quad (33)$$

Eqs. 26 and 27 can thus be generalised into the principal deviatoric stress increments as

$$\Delta s_i = \frac{\Delta\rho_s}{\Delta\rho_e} \Delta e_i \quad (34)$$

and, accordingly, into the deviatoric stress-tensor increments as

$$\Delta s_{ij} = \frac{\Delta\rho_s}{\Delta\rho_e} \Delta e_{ij}. \quad (35)$$

Now, considering the effective stresses and strains as invariant scalar equivalents of the deviatoric stress-tensor components [15] and deducing the effective trial stress increment $\Delta\sigma_{\text{eff}}^t$ as

$$\Delta\sigma_{\text{eff}}^t = 3G(T^{(2)}) \Delta\varepsilon_{\text{eff}}, \quad (36)$$

the ratio $\frac{\Delta\rho_s}{\Delta\rho_e}$ can be expressed from Eq. 35 in terms of the shear modulus $G(T^{(2)})$, the effective stress increment $\Delta\sigma_{\text{eff}}$ and the effective trial stress increment $\Delta\sigma_{\text{eff}}^t$ as

$$\frac{\Delta\rho_s}{\Delta\rho_e} = 2G(T^{(2)}) \frac{\Delta\sigma_{\text{eff}}}{\Delta\sigma_{\text{eff}}^t}, \quad (37)$$

which can also be written in terms of Lamé constant $\mu^*(T^{(2)})$ as

$$\frac{\Delta\rho_s}{\Delta\rho_e} = 2\mu^*(T^{(2)}). \quad (38)$$

Finally, joining the deviatoric stress-tensor increment given in Eq. 35 with the hydrostatic stress-tensor increment, the exact closed-form expression for the stress-tensor increment can be composed as

$$\Delta\sigma_{ij} = 2\mu^*(T^{(2)}) \Delta\varepsilon_{ij} + \lambda^*(T^{(2)}) \Delta\varepsilon_{kk} \delta_{ij}. \quad (39)$$

In Eq. 39, the coefficients $\mu^*(T^{(2)})$ and $\lambda^*(T^{(2)})$ stand for the Lamé constants defined as

$$\mu^*(T^{(2)}) = G(T^{(2)}) \frac{\Delta\sigma_{\text{eff}}}{\Delta\sigma_{\text{eff}}^t} \text{ and } \lambda^*(T^{(2)}) = K(T^{(2)}) - \frac{2}{3}\mu^*(T^{(2)}), \quad (40)$$

whereas the bulk modulus $K(T^{(2)})$ is expressed in terms of the Young's modulus $E(T^{(2)})$ and the Poisson's ratio $\nu(T^{(2)})$ as

$$K(T^{(2)}) = \frac{E(T^{(2)})}{3(1 - 2\nu(T^{(2)}))}. \quad (41)$$

If the point P does not reach the second yield function, Eq. 35 changes to $\Delta s_{ij} = 2G(T^{(2)}) \Delta e_{ij}$ with $\mu^*(T^{(2)}) = G(T^{(2)})$ so Eq. 39 transforms into Hooke's linear isotropic law for elastic solids.

2.2. Back-strain calculation

Unless a residual strain is present, the circular yield functions are all centred around zero, as shown in Fig. 3a. This usually, yet not necessarily, represents the initial (unloaded) state. If the point P does not exceed the second yield function with the radius q_2 , then the back-strains do not alter, so the material remains in the elastic region. However, if the point P moves beyond the second yield function, at least the second back-strain will change, and the material will enter the plastic region. The algorithm for the calculation of the radial stress increment according to Eq. 21 assumes that a radial move of the point P from the last accepted equilibrium state (1) to the current state (2), either moves the back-strains in the same radial direction or they remain at rest.

The back-strain calculation in the case of variable temperature with the graphical aid from Fig. 6 is as follows:

1. Initially, the position of the point P , which represents the elastic state of the material with index $l = 1$, changes from the last accepted equilibrium state (1) to the current state (2) due to the mechanical load and the temperature increment. This yields the first radial back-strain

$$E_{\rho 1}^{(2)} = e_{\rho}^{(2)} \quad (42)$$

and the first back-strain increment

$$\Delta \rho_{e1} = E_{\rho 1}^{(2)} - E_{\rho 1}^{(1)} = \Delta \rho_e. \quad (43)$$

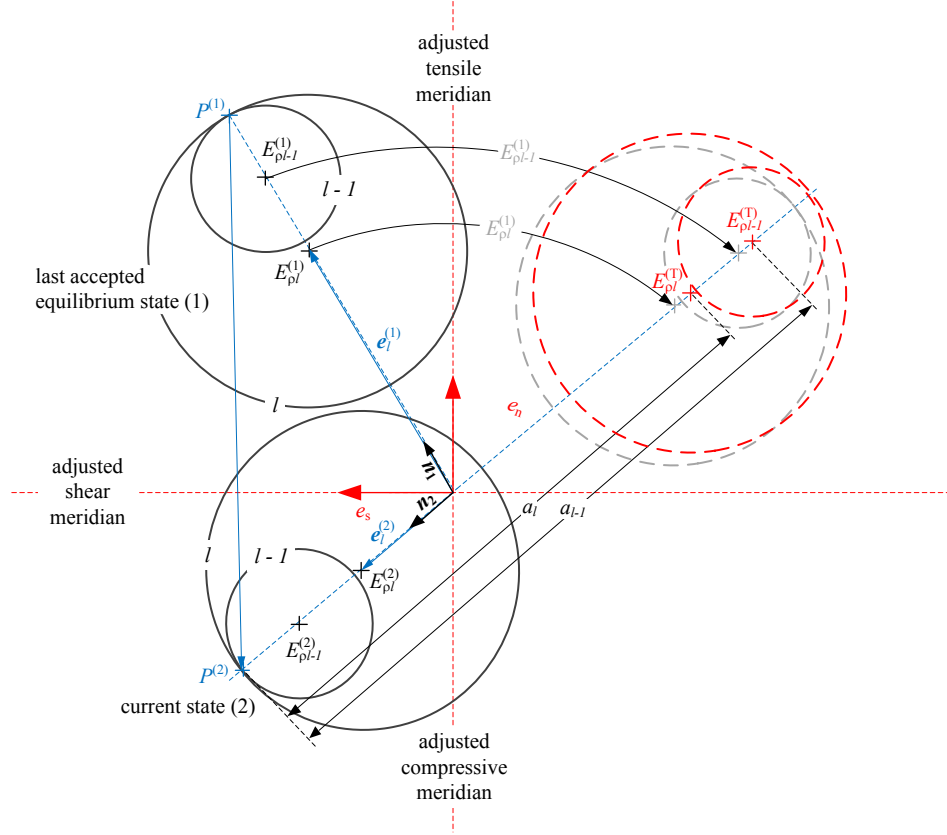


Figure 6: Back-strain calculation from the last accepted equilibrium state (1) to the current state (2).

Considering Eq. 42 and the calculation of $e_p^{(2)}$ from Eq. 12, the first radial back-strain $E_{\rho 1}^{(2)}$ is constituted with a positive and a negative sign in the regions of the tensile and compressive meridians, respectively. For a graphical representation of the positions of the plastic yield functions, a unit vector $\mathbf{n}_2 = [n_s, n_n]^\top$ can be computed, pointing in the direction of the point P in the current state (2). For the same reason, the positions of the plastic yield functions from the last accepted equilibrium state $E_{\rho l}^{(1)}$ (index $l > 1$) can be rotated into direction \mathbf{n}_2 .

2. Next, the positions of the plastic yield functions (index $l > 1$) are adjusted in order to take the temperature increment into account if $\Delta T \neq 0$ as

$$E_{\rho l}^{(T)} = \frac{\alpha_l(T^{(1)})}{\alpha_l(T^{(2)})} E_{\rho l}^{(1)} \quad \text{for } l = 2, \dots, n_q, \quad (44)$$

where $\alpha_l(T^{(1)})$ and $\alpha_l(T^{(2)})$ stand for the Prandtl densities at the last accepted equi-

librium state (1) and the current state (2), respectively.

3. Furthermore, the positions of the plastic yield functions (index $l > 1$) in the current state (2) are determined from the temperature-modified radial back-strains $E_{\rho l}^{(T)}$ and the current position of the point P (the radial back-strain $E_{\rho 1}^{(2)}$). The quantities a_l , which represent the radial movements between the current position of the point P and the temperature-modified positions of the points $E_{\rho l}^{(T)}$, can thus be calculated as

$$a_l = E_{\rho 1}^{(2)} - E_{\rho l}^{(T)} \quad \text{for } l = 2, \dots, n_q. \quad (45)$$

If $a_l > q_l$, then the l -th radial back-strain can be determined as

$$E_{\rho l}^{(2)} = E_{\rho 1}^{(2)} - q_l. \quad (46)$$

Otherwise, if $a_l < -q_l$, then the l -th radial back-strain is worked out as

$$E_{\rho l}^{(2)} = E_{\rho 1}^{(2)} + q_l, \quad (47)$$

or the value of the l -th radial back-strain is changed due to the temperature increment, so

$$E_{\rho l}^{(2)} = E_{\rho l}^{(T)}. \quad (48)$$

Finally, the l -th back-strain increment is calculated as

$$\Delta \rho_{el} = E_{\rho l}^{(2)} - E_{\rho l}^{(1)} \quad (49)$$

and the positions of the points $E_{\rho l}^{(2)}$ can be updated as

$$\mathbf{e}_l^{(1)} = |E_{\rho l}^{(2)}| \mathbf{n}_2. \quad (50)$$

The back-strain calculation in the case of constant temperature omits the second step of the procedure, so $E_{\rho l}^{(T)} = E_{\rho l}^{(1)}$ for $l = 2, \dots, n_q$. In either constant or variable temperature conditions, the back-strain calculation is carried out only for those yield functions where $e_{\max}^{(2)}$ from Eq. 15 is greater than the radius q_l . Both conditions significantly increase the computational power of the algorithm.

2.3. Material parameters

For the calculation of the Prandtl densities used in Eq. 21, either uniaxial cyclically stable tensile-compressive or cyclically stable pure-shear cyclic stress-strain curves are required. In the first case, only the σ_{11} component of the stress tensor is non-zero, whereas in the latter case, only the σ_{12} component of the stress tensor is non-zero. The curves are frequently, but not necessarily, approximated by the Ramberg-Osgood relation [6, 11, 35, 46, 54]. The use of the Ramberg-Osgood stress-strain relation is convenient due to its advantageous description of kinematic hardening at cyclic loading by only three parameters (E , K' and n'). However, the approach is not restrained to the Ramberg-Osgood curves. If a different stress-strain relationship is used, e.g. the Armstrong-Frederick or similar, the corresponding material parameters have to be determined [54]. Moreover, even individual stress-strain points at test temperatures can be provided as an input for the determination of the Prandtl densities [47]. For this study, the corresponding material parameters for ferritic stainless steel EN 1.4512 [6, 11, 46] are listed in Table 1, where E , K' and n' stand for elastic modulus and Ramberg Osgood's cyclic hardening coefficient and cyclic hardening exponent, respectively. Additionally, tensile strength R_m , proportional limit stress σ_p and the Poisson's ratio ν are also given for the test temperatures 20, 300 and 650 °C.

Table 1: Elastic modulus E , Ramberg–Osgood parameters K' and n' , tensile strength R_m , proportional limit stress σ_p and the Poisson's ratio ν for ferritic stainless steel EN 1.4512 used in this study.

T [°C]	E [MPa]	K' [MPa]	n' [-]	R_m [MPa]	σ_p [MPa]	ν [-]
20	200000	603.42	0.1211	407	140	0.3
300	180000	508.16	0.1103	360	120	0.3
650	150000	183.13	0.0336	165	90	0.3

Next, the cyclically stable cyclic stress-strain curves, obtained from either uniaxial tensile-compressive, low-cycle fatigue testing or incremental step testing [54, 55], are converted into

the radial stress in the deviatoric plane as

$$s_r = \sqrt{\frac{2}{3}}\sigma_{\text{eff}} \quad (51)$$

and the radial strain in the deviatoric plane as

$$e_r = \sqrt{\frac{3}{2}}\varepsilon_{\text{eff}}, \quad (52)$$

where the effective stress and the effective strain are given according to the definition [15] by

$$\sigma_{\text{eff}} = \sqrt{\frac{3}{2}s_{ij}s_{ij}} = \sigma_{11} \quad \text{and} \quad \varepsilon_{\text{eff}} = \sqrt{\frac{2}{3}e_{ij}e_{ij}} = \varepsilon_{\text{eff}}^e + \varepsilon_{\text{eff}}^p = \frac{\sigma_{\text{eff}}}{3G} + \varepsilon_{11}^p, \quad (53)$$

respectively. If the cyclic stress-strain curve is described by the Ramberg–Osgood relation, the plastic strain component ε_{11}^p equals

$$\varepsilon_{11}^p = (\sigma_{11}/K')^{1/n'}. \quad (54)$$

If the pure-shear, cyclically stable, cyclic stress-strain curves are available, then the curves are converted into shear stress and strain in the deviatoric plane according to Eqs. 51 and 52, only now the effective stress and effective strain are given by

$$\sigma_{\text{eff}} = \sqrt{3}\sigma_{12} \quad \text{and} \quad \varepsilon_{\text{eff}} = \varepsilon_{\text{eff}}^e + \varepsilon_{\text{eff}}^p = \frac{\sigma_{\text{eff}}}{3G} + \frac{1}{\sqrt{3}}\gamma_{12}^p. \quad (55)$$

For the Ramberg–Osgood relation, the engineering plastic strain γ_{12}^p is calculated as

$$\gamma_{12}^p = 2\varepsilon_{12}^p = (\sigma_{12}/K')^{1/n'}. \quad (56)$$

The cyclically stable, cyclic radial stress-strain curves in the deviatoric plane for the EN 1.4512 steel are depicted in Fig. 7.

The radius of the first circular yield function q_1 is always set to zero, whereas the radius of the second circular yield function equals

$$q_2 = \min_T \sqrt{\frac{3}{2}} \left(\frac{\sigma_p(T)}{3G(T)} + \left(\frac{\sigma_p(T)}{K'(T)} \right)^{\frac{1}{n'(T)}} \right) \quad (57)$$

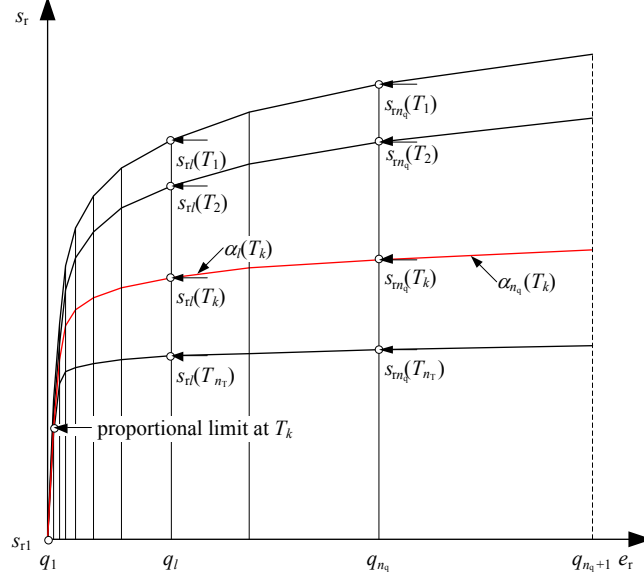


Figure 7: Temperature-dependent, cyclically stable, cyclic radial stress-strain curves in the deviatoric plane for EN 1.4512 steel.

and the radius of the last circular yield function is given as

$$q_{n_q+1} = \max_T \sqrt{\frac{3}{2}} \left(\frac{R_m(T)}{3G(T)} + \left(\frac{R_m(T)}{K'(T)} \right)^{\frac{1}{n'(T)}} \right). \quad (58)$$

For the material data of the EN 1.4512 steel given in Table 1, both q_2 and q_{n_q+1} correspond to the highest test temperature $T = 650^\circ\text{C}$. The radii of the intermediate circular yield functions are distributed between q_2 and q_{n_q+1} , as shown in Fig. 7. When the data pairs q_l and $s_{rl}(T)$ are known, the Prandtl densities $\alpha_l(T)$ for $l = 1, \dots, n_q$ are calculated as

$$\alpha_l(T) = \frac{1}{q_{l+1} - q_l} (s_{rl+1}(T) - \sum_{\tilde{l}=1}^{l-1} \alpha_{\tilde{l}}(T)(q_{l+1} - q_{\tilde{l}})). \quad (59)$$

The radius of the last circular yield function becomes excessive when the Prandtl densities in Eq. 59 are known, so hereafter q_{n_q+1} is deleted. The Prandtl densities are calculated for the set of n_T uniformly distributed temperatures between the minimum (20°C) and the maximum (650°C) test temperature. They are stored together with the yield radii prior to the start of the simulation in order to retain a high computational speed. The radial stress in the deviatoric plane s_r in Eq. 59 depends on the material parameters for the interpolated

temperatures. Hence, $E(T)$, $K'(T)$, $n'(T)$, $R_m(T)$, $\sigma_p(T)$ and $\nu(T)$ have to be pre-calculated for the given set of n_T temperatures, as given, e.g. in [41–46].

2.4. Consistent material Jacobian

A structural elastoplastic analysis using an implicit finite element method performs accurately and quickly only if the material sensitivity in terms of $\frac{\partial \Delta \sigma}{\partial \Delta \varepsilon}$ is ensured consistently [12, 56].

Hence, the material Jacobian is defined here for the closed-form elastoplastic solution using the Prandtl operator approach, as required in finite element solvers, e.g. the Abaqus user material programme code UMAT. Starting from Eq. 21, it can be shown that $\Delta \rho_s$ is a linear function of $\Delta \rho_e$. The slope depends on the Prandtl densities $\alpha_l(T^{(2)})$, whereas the intercept additionally depends on the back-strains $E_{\rho l}^{(1)}$ and the Prandtl densities $\alpha_l(T^{(1)})$. By applying the differential operator δ to a single segment of the Prandtl model, Eq. 21 yields

$$\delta \Delta \rho_{sl} = \alpha_l(T^{(2)}) \delta \Delta \rho_e \quad (60)$$

if the l -th radial back-strain $E_{\rho l}^{(2)}$ changes according to Eqs. 46 or 47. If $E_{\rho l}^{(2)}$ changes according to Eq. 48, the application of the differential operator δ to a single segment of the Prandtl model in Eq. 21 results in

$$\delta \Delta \rho_{sl} = 0. \quad (61)$$

The differential stress increment $\delta \Delta \rho_s$ can now be expressed as

$$\delta \Delta \rho_s = \sum_{l=1}^{n_q} \delta \Delta \rho_{sl} = \alpha^*(T^{(2)}) \delta \Delta \rho_e, \quad (62)$$

where $\alpha^*(T^{(2)})$ sums up the contributions from Eqs. 60 and 61.

Again, considering the effective stresses and strains as invariant scalar equivalents of the deviatoric stress-tensor components [15], the differential effective-stress increment is obtained as

$$\delta \Delta \sigma_{\text{eff}} = \frac{3}{2} \alpha^*(T^{(2)}) \delta \Delta \varepsilon_{\text{eff}}. \quad (63)$$

Introducing the trial deviatoric stress-tensor increment Δs_{ij}^t , as

$$\Delta s_{ij}^t = 2G (T^{(2)}) \Delta e_{ij}, \quad (64)$$

while considering the effective trial-stress increment from Eq. 36 and the effective strain increment $\Delta \varepsilon_{\text{eff}}$ as

$$\Delta \varepsilon_{\text{eff}} = \sqrt{\frac{2}{3} \Delta e_{ij} \Delta e_{ij}}, \quad (65)$$

the application of the differential operator yields

$$\delta \Delta \varepsilon_{\text{eff}} = \frac{\Delta s_{ij}^t}{\Delta \sigma_{\text{eff}}^t} \delta \Delta e_{ij} = \eta_{ij}(T^{(2)}) \delta \Delta e_{ij}, \quad (66)$$

where η_{ij} stands for

$$\eta_{ij} = \frac{\Delta s_{ij}^t}{\Delta \sigma_{\text{eff}}^t}. \quad (67)$$

Similarly, considering the definition of the effective trial-stress increment $\Delta \sigma_{\text{eff}}^t$ as

$$\Delta \sigma_{\text{eff}}^t = \sqrt{\frac{3}{2} \Delta s_{ij}^t \Delta s_{ij}^t}, \quad (68)$$

the differential operator gives

$$\delta \Delta \sigma_{\text{eff}}^t = 3G (T^{(2)}) \eta_{ij}(T^{(2)}) \delta \Delta e_{ij}. \quad (69)$$

Moreover, applying the differential operator to deviatoric stress-tensor increments in Eq. 35, while considering the ratio $\frac{\Delta \rho_s}{\Delta \rho_e}$ from Eq. 37, the differential deviatoric stress-tensor increments can be gained as

$$\delta \Delta s_{ij} = 2\mu^* (T^{(2)}) \delta \Delta e_{ij} + \left(\frac{3}{2} \alpha^* (T^{(2)}) - 3\mu^* (T^{(2)}) \right) \eta_{ij}(T^{(2)}) \eta_{kl}(T^{(2)}) \delta \Delta e_{kl}. \quad (70)$$

Finally, considering Eq. 6 and acknowledging

$$\Delta s_{ij} = \Delta \sigma_{ij} - \frac{1}{3} \Delta \sigma_{kk} \delta_{ij} \quad (71)$$

the exact, closed-form expression for the consistent material Jacobian is derived as

$$\delta \Delta \sigma_{ij} = 2\mu^* (T^{(2)}) \delta \Delta \varepsilon_{ij} + \lambda^* (T^{(2)}) \delta_{ij} \delta \Delta \varepsilon_{kk} + \left(\frac{3}{2} \alpha^* (T^{(2)}) - 3\mu^* (T^{(2)}) \right) \eta_{ij}(T^{(2)}) \eta_{kl}(T^{(2)}) \delta \Delta \varepsilon_{kl}. \quad (72)$$

In the case of elasticity where $\alpha^*(T^{(2)}) = \alpha_1(T^{(2)}) = 2G(T^{(2)})$ and $\mu^*(T^{(2)}) = G(T^{(2)})$, Eq. 72 turns into the consistent material Jacobian for Hooke's linear isotropic law as

$$\delta\Delta\sigma_{ij} = 2G(T^{(2)})\delta\Delta\varepsilon_{ij} + \left(K(T^{(2)}) - \frac{2}{3}G(T^{(2)})\right)\delta_{ij}\delta\Delta\varepsilon_{kk}. \quad (73)$$

The stability of the procedure depends on the ratio $\frac{\Delta\rho_s}{\Delta\rho_e}$ in Eq. 38. If $\left|\frac{\Delta\rho_s}{\Delta\rho_e}\right| > \alpha_1(T^{(2)})$, then

$$\frac{\Delta\rho_s}{\Delta\rho_e} = \alpha_1(T^{(2)}) \quad (74)$$

and

$$\alpha^*(T^{(2)}) = \alpha_1(T^{(2)}). \quad (75)$$

3. Results and discussion

The presented closed-form solution for structural elastoplastic analyses was implemented into an Abaqus UMAT routine and tested on several load cases. The material parameters for the ferritic stainless steel EN 1.4512 were used for the simulations, given in Table 1. The experimental stress-strain range was divided into 33 yield functions, whereas the experimental temperature range was divided into 500 steps between the minimum and the maximum test temperatures. Initially, the stress-strain response of a single linear *C3D8*-type structural finite element was simulated against two variable tensile-compressive thermomechanical load histories, given in Figs. 8a and 8b. While the thermal load was equal for both load histories, the mechanical load was applied as displacements in the first load history and as forces in the second load history.

Next, the stress-strain response was simulated for two variable shear thermomechanical load histories (Figs. 8c and 8d). The thermal load was equal for both shear load histories, while the mechanical loads were applied either as displacements or forces. Furthermore, the simulations on a single finite element were repeated for an initially distorted finite element. Finally, a rectangular cross-sectioned cantilever beam, composed of 750 linear *C3D8*-type finite elements and 1224 nodes, was exposed to two variable thermomechanical load histories,

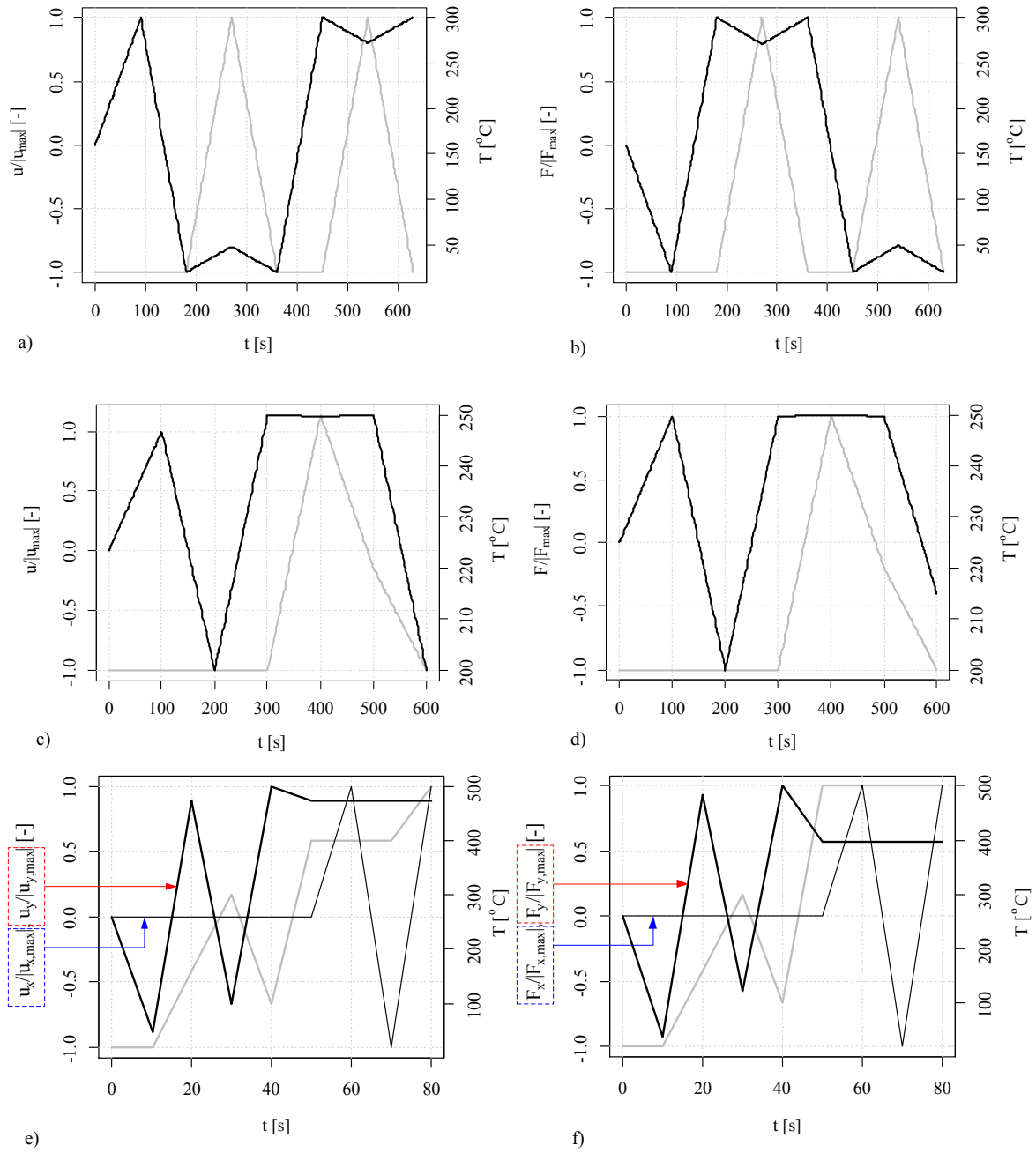


Figure 8: Thermomechanical load histories for a) displacement-controlled tension-compression of a single finite element, b) force-controlled tension-compression of a single finite element, c) displacement-controlled shear of a single finite element, d) force-controlled shear of a single finite element, e) displacement-controlled load of a cantilever beam and f) force-controlled load of a cantilever beam. Black solid lines represent the mechanical load and the grey solid lines represent the thermal load.

given in Figs. 8e and 8f. One end of the cantilever beam was fixed, and the other end of the cantilever beam was loaded by either a displacement or a force, whereas the thermal load was applied uniformly over the whole finite element model. Moreover, the mechanical load was applied in two directions to introduce a non-proportional loading sequence. For this reason, the cantilever beam was initially mechanically loaded in y-direction between 0 and 50 s (Figs. 8e and 8f.) Between 50 and 80 s, mechanical load in x-direction was added. The stress-strain response of the cantilever beam was simulated for the applied conditions.

The results of the simulations using the implemented Prandtl model were compared with the results using the Besseling model (from here on the reference model), which also enables structural analyses of mechanical components subjected to variable thermomechanical load histories considering a cyclic elastoplastic behaviour with multilinear kinematic hardening. The models have been compared in terms of the simulated stress-strain behaviour and the computational time needed to complete the analyses.

3.1. Tensile-compressive response of a single finite element

The results of the simulation for a single finite element subjected to two variable tensile-compressive thermomechanical load histories are given in Fig. 9. It is clear that the stress-strain simulation using the Prandtl model corroborates with the results of the simulation using the reference model. For each of the given load histories, a major hysteresis loop emerges with a minor loop at each reversal point. The major hysteresis loop is created between the reversal points at 90 s, 180 s and 450 s and at 20 °C, whereas the minor loops are created between the time intervals 180 s to 360 s and 450 s to 630 s, where the temperature changes between 20 °C and 300 °C. The major hysteresis loops are hardly distinguishable from the models, which confirms the suitability of the proposed methodology using the Prandtl operator approach. However, small discrepancies can be obtained, mostly during the minor loops, suggesting a different consideration of the temperature influence in the models. They can also be recognised in Figs. 10a and 10b between the time intervals 180 s to 360 s and 450 s to 630 s. Although the size of the temperature step and the interpolation between the experimental cyclic curves to determine the material parameters for the non-

experimental temperatures can influence the results of the simulations using the Prandtl model, the correlation with the reference model is noteworthy.

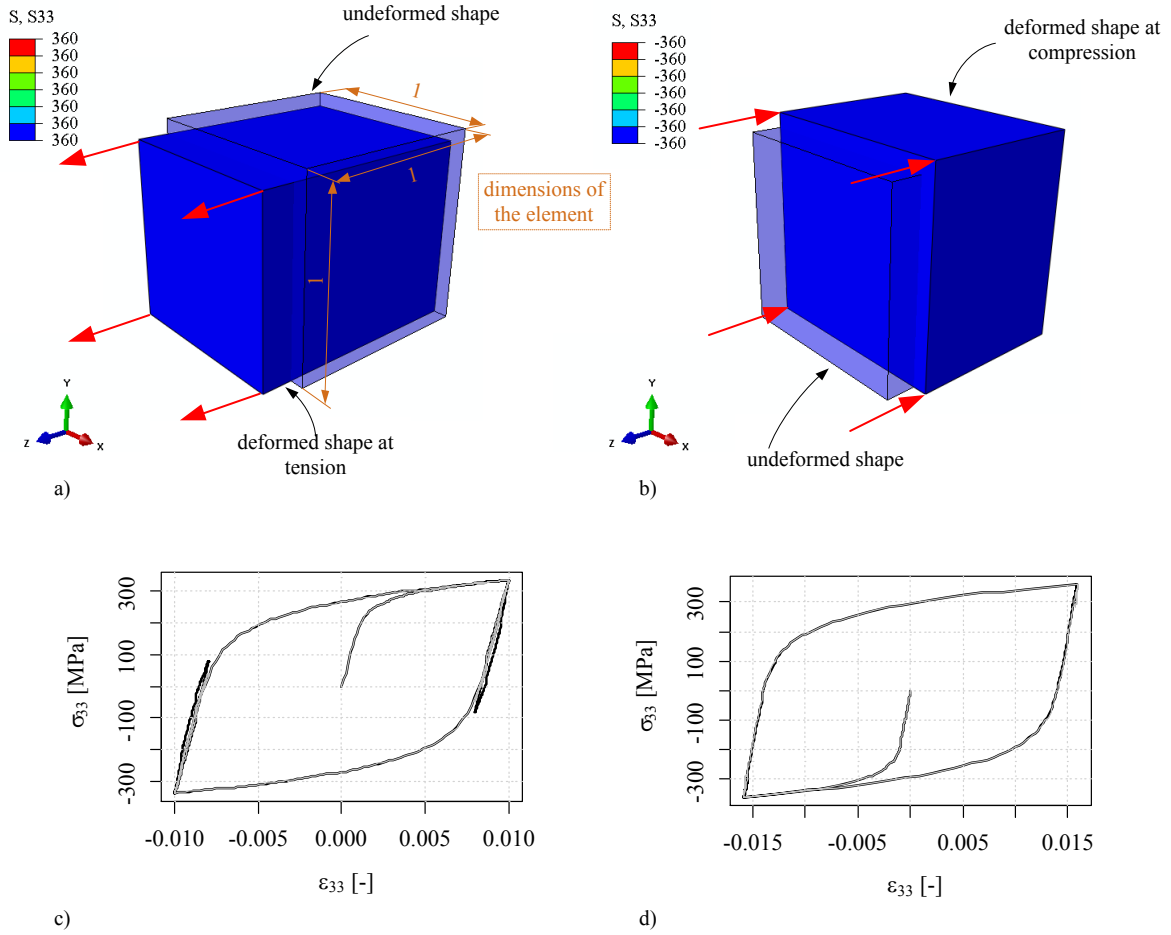


Figure 9: Single finite element subjected to a) tensile loading and b) compressive loading, c) corresponding stress-strain response of displacement-controlled load and d) corresponding stress-strain response of force-controlled load. The shape change of the finite element is magnified by a factor of 10. Thick black lines represent the Prandtl model and thin grey lines represent the reference model.

The tensile-compressive loading in the z-direction only affects the σ_{33} component of the stress tensor (Fig. 9). The cause of the movement of the back-strains $E_{\rho l}$ is hence the thermomechanical excitation in the z-direction (Fig. 11). Initially, there are no residual back-strains; therefore, consequent segments of the Prandtl model are being activated gradually up to 90 s. A linear incremental changing of the displacement-controlled loading between

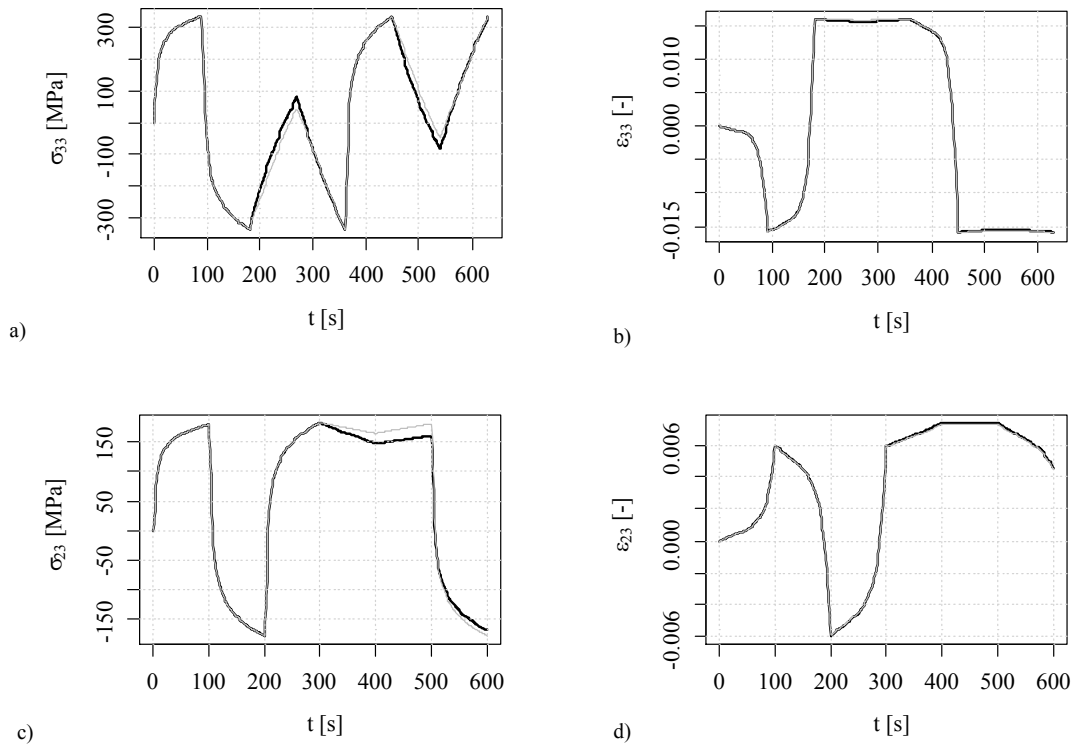


Figure 10: a) Stress signal of displacement-controlled tensile-compressive load history, b) strain signal of force-controlled tensile-compressive load history, c) stress signal of displacement-controlled shear load history and d) strain signal of force-controlled shear load history. Thick black lines represent the Prandtl model and thin grey lines represent the reference model.

the reversal points generates a linear movement of the back-strains (Fig. 11a), whereas a linear incremental changing of the force-controlled loading results in the nonlinear behaviour of the back-strains due to the nonlinear relationship between the stresses and the strains in the material model (Fig. 11b). The positions of the back-strains at the reversal points of the major hysteresis loop are demonstrated at 90 s, 180 s and 450 s. The yield surfaces with larger radii activate with a delay, which exhibits the properties of the memory rules. However, the temperature change causes a rearrangement of the back-strains according to Eq. 44, which can be seen between the time intervals 180 s to 360 s and 450 s to 630 s. Since the yield functions are mutually independent, a decoupled rearrangement of the back-strains emerges depending on the ratio between the Prandtl densities at the temperature of the last accepted equilibrium state and at the current state. Importantly, a reversible temperature-dependent rearrangement is observed at 360 s and 630 s, so the back-strains shift back to the positions before the temperature change if no additional load is applied during the heating-up and cooling-down processes.

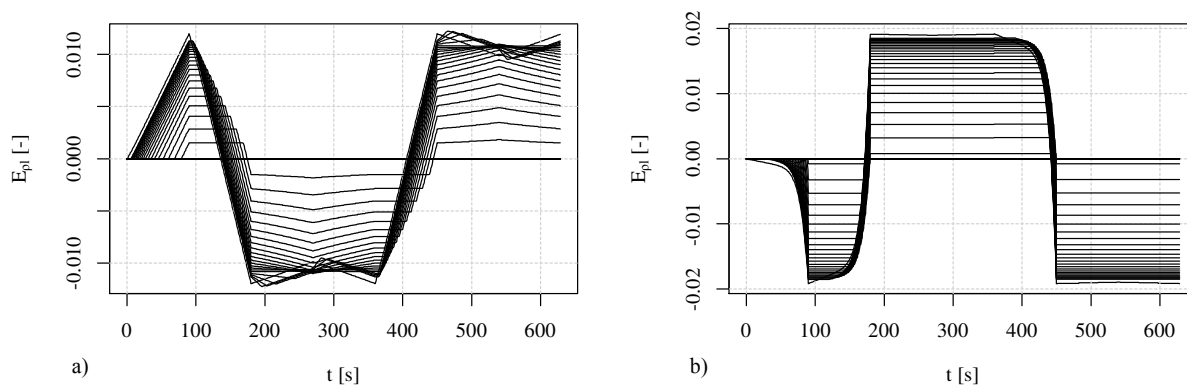


Figure 11: Positions of the back-strains during tensile-compressive a) displacement-controlled and b) force-controlled loading of a single finite element.

3.2. Shear response of a single finite element

The results of a single finite element, exposed to variable shear thermomechanical load histories, are presented in Fig. 12. It is clear that only the shape changes during this type of loading, while the volume remains unmodified. Once more, the stress-strain simulation

using the Prandtl model shows noticeable agreement with the reference model. The major hysteresis loop that appears between 100 s and 300 s is scarcely distinguishable from the models (Figs. 12c, 12d, 10c and 10d). A slight discordance is again observed during the temperature change between 300 s and 600 s for the same reasons as for the tensile-compressive loading.

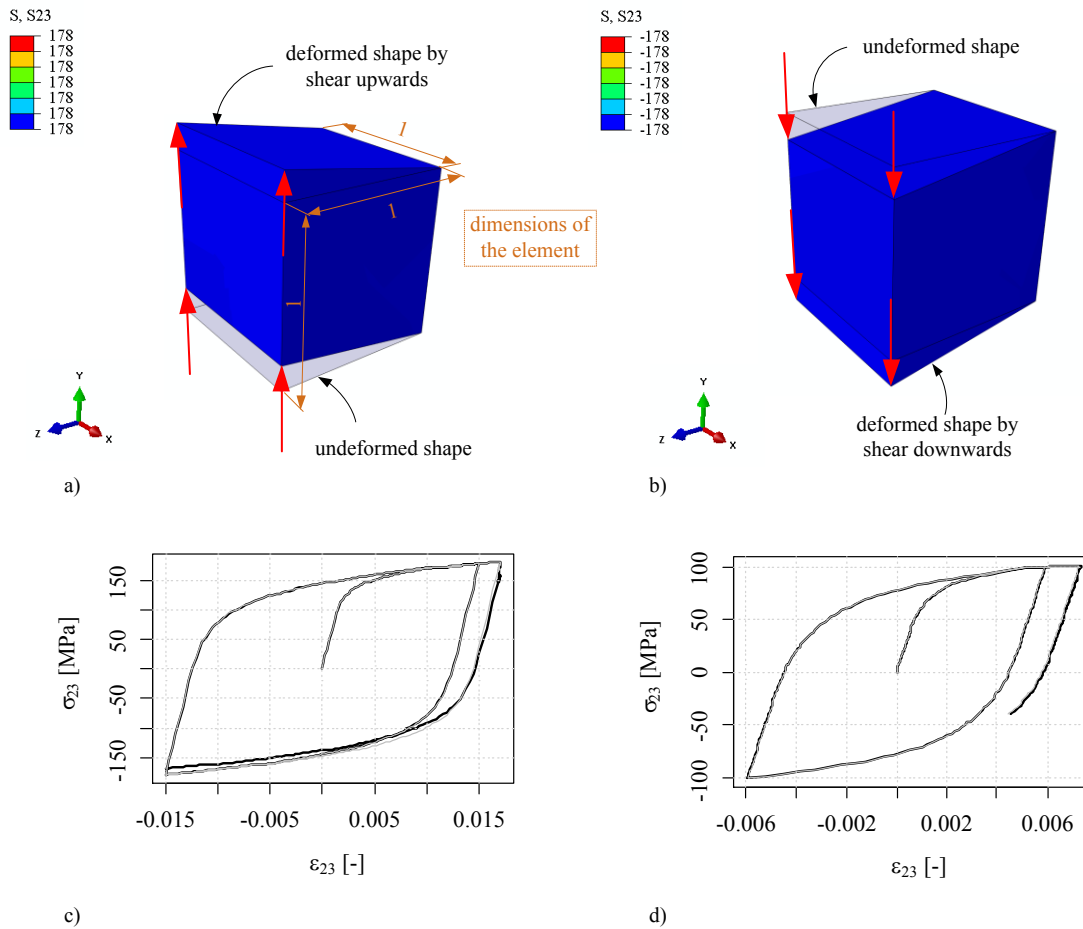


Figure 12: Single finite element subjected to a) shear loading in positive y-direction and b) shear loading in negative y-direction, c) corresponding stress-strain response of displacement-controlled load and d) corresponding stress-strain response of force-controlled load. Thick black lines represent the Prandtl model and thin grey lines represent the reference model.

The movements of the back-strains appear due to the thermomechanical shear loading in the y-direction (Fig. 13). After the unloaded state, the back-strains activate gradually and

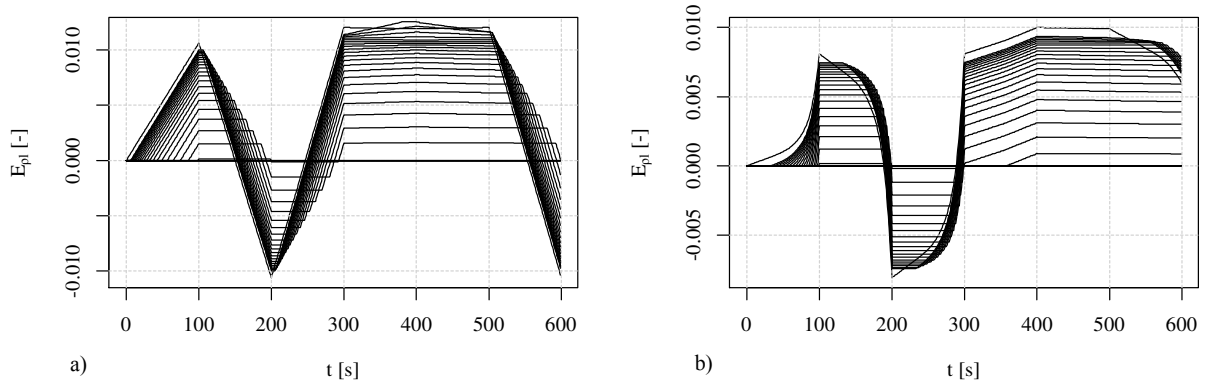


Figure 13: Positions of the back-strains during shear a) displacement-controlled and b) force-controlled loading of a single finite element.

change the direction of their movement at the reversal points of the major hysteresis loop, as depicted at 100, 200 and 300 s. A nonlinear movement of the back-strains is observed during the linear incremental force-controlled shear loading (Fig. 13b). The temperature change causes a rearrangement of the yield functions after 300 s; however, this does not reverse completely at 500 s, as also the temperature does not yet return to the initial temperature at that time.

3.3. Response of a single initially distorted finite element

The results of a single initially distorted finite element, exposed to variable shear thermomechanical load histories, are presented in Fig. 14. An initially distorted shape with the aspect ratio of 6.04 and the maximum angle of 162.6° has been chosen to perform the calculations. The element was subjected to the same loading as the non-distorted (regular) element under the displacement control. However, in order to meet a converged solution also for the reference model, the amplitudes of the force-controlled loading were reduced due to a smaller cross-section of the distorted element. Namely, the slope of the stress-strain curve of the reference model is considered as a horizontal line beyond the last input stress-strain point whereas the last slope is maintained beyond the last yield strain in the case of the Prandtl operator approach. If the loading exceeds the last input stress-strain point of the reference model, the material behaves as ideally plastic, i.e. in the case of a single element,

the force-controlled load cases will not converge.

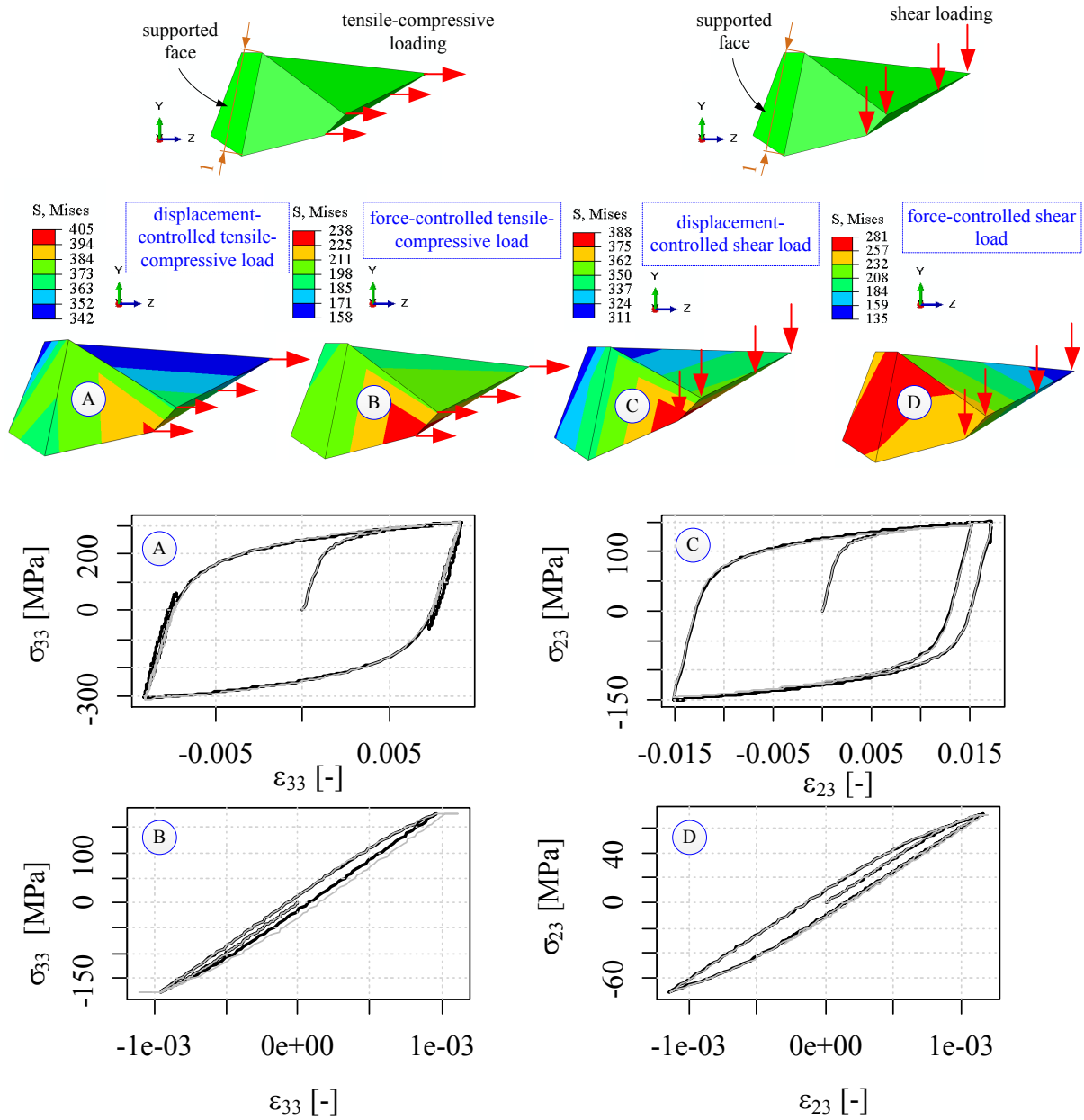


Figure 14: Analysis of an initially distorted single element subjected to tensile-compressive and shear loading. The deformed shapes, magnified by a factor of 10, are depicted after the first load step (10 s).

For the comparison, the same quantities were chosen as in the case of the non-distorted

element and compared against the reference model (Fig. 14). Due to the distorted shape, a multiaxial stress-strain response appears in all load cases which reduces the yielding in individual components (equivalent von Mises stress in Fig. 14). Hence the results of the initially distorted element cannot directly be compared to the results of the non-distorted element. Nevertheless, the results can be compared between the material models. Even in the case of an initially distorted element, a good agreement between the Prandtl and the reference models can be obtained. Some discrepancies appear during the minor loops which, as in the case of the non-distorted element, can be attributed to a different consideration of the temperature influence in the models.

3.4. Response of a cantilever beam

The results of the simulations of a cantilever beam subjected to variable thermomechanical load histories are depicted in Figs. 15, 16 and 17. The dimensions of the cantilever beam are given in Fig. 15.

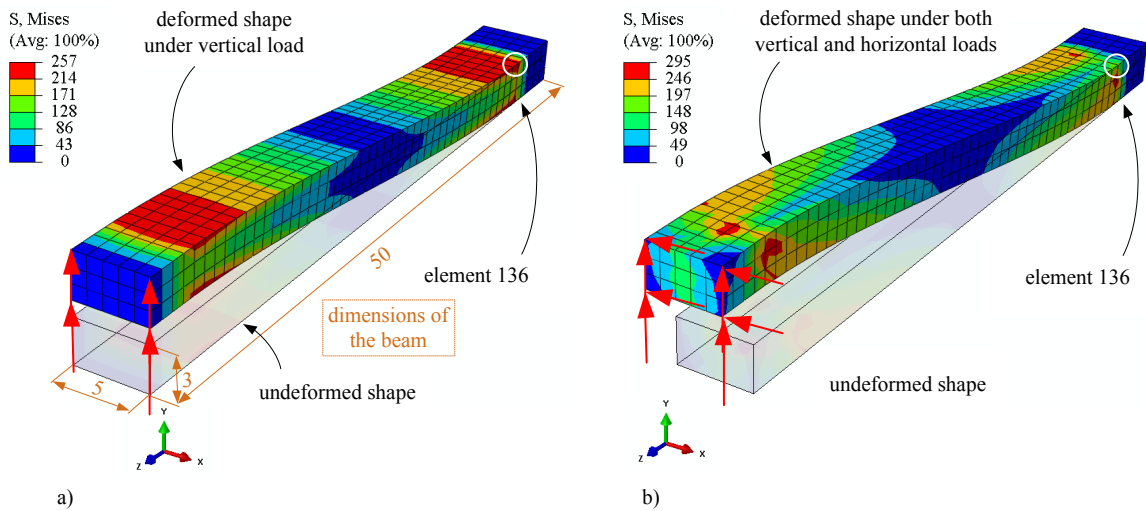


Figure 15: Cantilever beam subjected to variable loading a) in y -direction ($t = 10$ s) and b) x and y -directions ($t = 70$ s). The shape change of the finite element model is magnified for a factor of 10.

In the first 40 s, the cantilever beam was loaded mechanically in the y -direction (Fig. 15a) and after a considerable temperature rise between 40 s and 50 s (Figs. 8e and 8f), a mechanical load was added in the x -direction (Fig. 15b). A finite element close to the fixed support

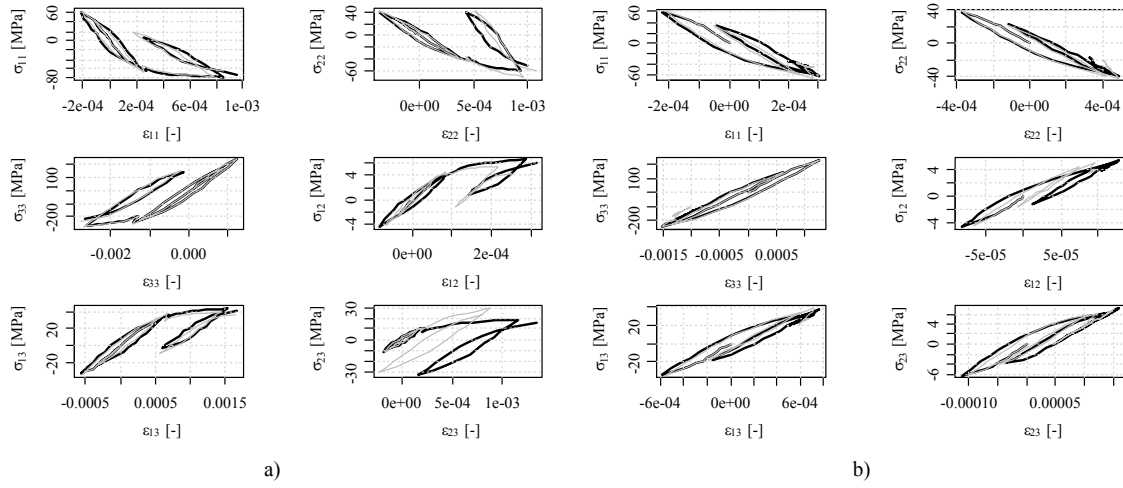


Figure 16: Stress-strain tensor components in element 136 of the cantilever beam for a) displacement-controlled and b) force-controlled load histories. Thick black lines represent the Prandtl model and thin grey lines represent the reference model.

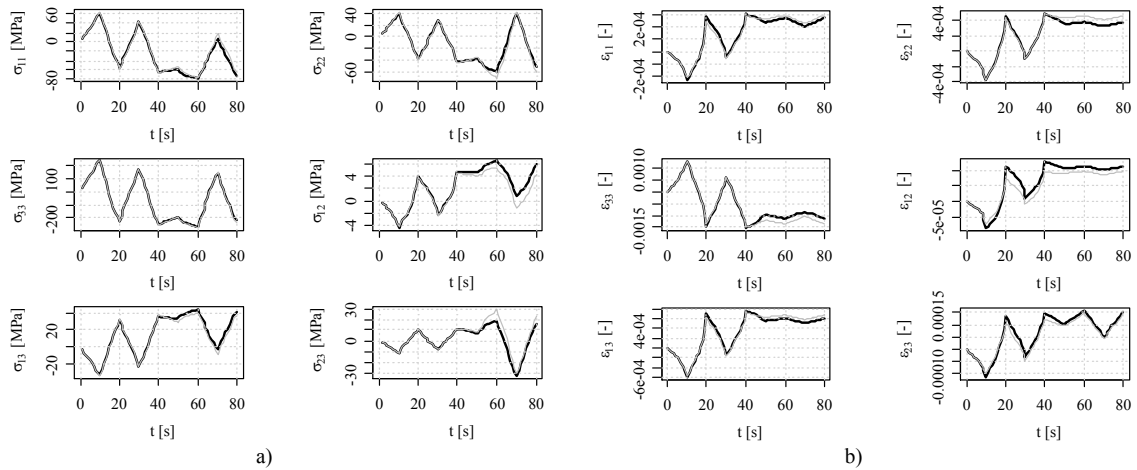


Figure 17: Signal in element 136 of the cantilever beam for a) stress tensor components during displacement-controlled load history and b) strain tensor components during force-controlled load history. Thick black lines represent the Prandtl model and thin grey lines represent the reference model.

of the cantilever beam was chosen to display the results of the stress-strain simulations. The reason being that close to the support, high values of the stresses and strains were expected. This element is marked as element 136 in Fig. 15. Generally speaking, good agreement between the results using the Prandtl and the reference model was found, as shown in Figs. 16 and 17. Although all the components of both the stress and the strain tensors are depicted, they can be divided by the absolute values of the stresses or strains for the purposes of the discussion. For example, the stress component σ_{33} is considerably higher than the stress components σ_{13} or σ_{12} . Significantly, the result of the simulation using the Prandtl model correlates favourably for the highest component of the stress-strain tensor with the reference model in either displacement-controlled or force-controlled loading. The highest discrepancy between the models can be noted for the components σ_{23} and ε_{23} , although especially in the case of the force-controlled loading the absolute values of the stress and strain tensor are low. Other components of the stress-strain response match notably also during the variable temperature until 40 s, but can differ to some extent after the major temperature rise between 40 s and 50 s. The reasons for the discrepancies lie in the different temperature behaviours of the models, as already stated above. This effect is now even more pronounced in the analysed finite element of the cantilever beam than during the simulations on a single finite element since the discrepancies on each finite element between the position of the load input onto the cantilever beam and the position of the element 136 intensify.

In the case of variable displacement-controlled or force-controlled loads on the cantilever beam, the back-strains fluctuate due to the complex changing of all the components of the strain tensor and the temperature (shown for element 136 in Fig. 18). In the first 40 s, the back-strains are gradually activated, although their slopes differ during their movement between the reversal points. The difference in the slopes is the effect of the variable temperature during this time interval. Furthermore, a large temperature change after 40 s causes a rise in the rearrangement of the back-strains. Moreover, the loading in both the x and y-directions after 50 s activates additional yield surfaces with larger radii, which is more pronounced in the case of the displacement-controlled loading.

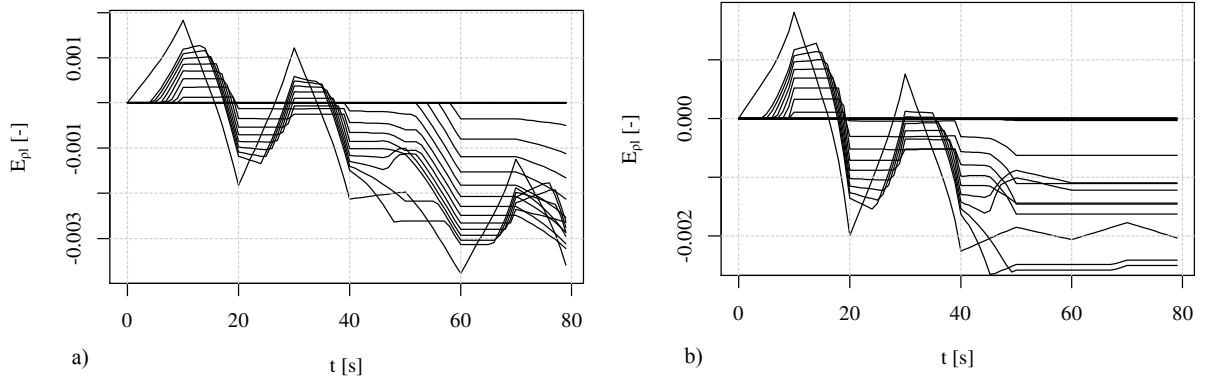


Figure 18: Positions of the back-strains in element 136 during a) displacement-controlled and b) force-controlled loading of the cantilever beam.

3.5. Computational power

The main advantage of the closed-form solution for the description of the cyclic elastoplastic behaviour with multilinear temperature-dependent kinematic hardening is in the removal of the iterative procedure for determining the stress tensor's increment. Since the iterative procedure is time consuming, the improvement of the closed-form solution is the increase of the computational power of the method. To evaluate and compare the computational power of the Prandtl and the reference models, the computational times were measured to conduct the analysis. Moreover, the time of the central processing unit (CPU time) and the wall-clock time were assessed, and are presented in Table 2. The simulations were performed on an Intel Core i7-4710MQ quad core 2.5-GHz processor with 8 GB of DDR SDRAM. The most striking result to emerge from the comparison of the values of either the CPU time or the wall-clock time from Table 2 is that the computational power of the Prandtl model becomes clear with the increasing complexity of the analysis. Specifically, the computational times for the cantilever beam can be up to 45 % shorter when using the Prandtl model than when using the reference model. In addition, for the simulations of tensile-compressive and shear loadings on a single finite element, comparable computational times were observed using the Prandtl or the reference model. Consistently, similar values for the decrease of the computational times have been observed as in [11], where the Prandtl

operator approach was implemented in an elastic predictorplastic corrector procedure. In agreement with the presented closed-form solution of elastoplasticity, the simulations are also substantially accelerated by identifying a constant temperature field during a single load step or controlling the highest strain achieved at every integration point. If a given yield function is not reached, the calculation of the back-strains in Eq. 44 and the summation in Eq. 21 are interrupted, as the positions of the back-strains for the subsequent yield functions could not have moved. Another notable observation is the identification of either the elastic region of the material. The convergence of the analyses was generally achieved in a single iteration for every prescribed time increment. However, due to the complex exchange of the thermal and mechanical load histories, numerical difficulties can arise during the simulations, which was also observed when using the Besseling model. In such cases, the convergence stability of the Prandtl operator approach can be controlled by the ratio $\frac{\Delta\rho_s}{\Delta\rho_e}$ according to Eqs. 74 and 75. Comparison of the computational time difference for various sizes of finite elements (Fig. 19) reveals an increasing difference in favour of the Prandtl operator approach from the coarsest mesh of 13 finite elements with the size of 4 mm (load cases A_u and A_F in Fig. 19) up to the fine mesh of 750 finite elements with the size of 1 mm (load cases C_u and C_F in Fig. 19). Here, the computational times differ for 33 % in the case of the displacement-controlled load and for 45 % in the case of the force-controlled load. The computational power of the Prandtl operator approach then moderately reduces for the simulation with the finest mesh of 6000 finite elements with the size of 0.5 mm (load cases D_u and D_F).

There are some limitations of the current version of the Prandtl operator approach which are already a subject of the on-going research. The movements of the yield surfaces and consequently the radial strain increments are controlled by the values of the second and third deviatoric strain-invariant increments (Eqs. 7 and 8). In the case of extremely low values of the third deviatoric strain-invariant increments, the directions of movement of the yield surfaces are changed at the start of each load step by assigning the opposite sign to the radial strain increments. Moreover, the number of iterations outside the material point level depends on the treatment of the ratio $\frac{\Delta\rho_s}{\Delta\rho_e}$ as given in Eqs. 74 and 75, too. Furthermore, it

Table 2: Comparison of the computational times using the Prandtl and reference models for 1-mm finite elements.

Example	CPU time [s]		Wall-clock time [s]	
	Prandtl	Ref. model	Prandtl	Ref. model
Single element - displacement-controlled tensile-compressive load	12.8	13.0	13	13
Single element - force-controlled tensile-compressive load	12.9	12.8	13	13
Single element - displacement-controlled shear load	11.6	11.3	12	12
Single element - force-controlled shear load	12.6	12.6	13	14
Cantilever beam - displacement-controlled load	22.0	32.8	22	33
Cantilever beam - force-controlled load	17.2	31.5	17	33

is important how the cyclic stress-strain curves are discretised. Namely, the discretisation of the cyclic stress-strain curves at available test temperatures determines the values of the Prandtl densities at all temperatures, including the test and the interpolated temperatures. An optimal position of the yield strains ensures numerical stability during changeable temperature conditions. The calculation of the optimal position remains a challenge for the future studies. Moreover, the required number of iterations to observe a converged solution is influenced by the definition of the consistent material Jacobian. If the consistent material Jacobian is calculated using the shear strains according to Eq. 72, then the resulting matrix has a symmetric form. If engineering shear strains are provided instead, as it is usually the case in finite element solvers, then the consistent material Jacobian results in an unsymmetric form. An unsymmetric material Jacobian hence unnecessarily increases the computational time. However, the use of the generally faster symmetric form, when the unsymmetric form is mandatory, results in the erroneous estimation of the $\frac{\partial \Delta \sigma}{\partial \Delta \epsilon}$ which then influences the computational time and convergence. Linear three-dimensional structural finite elements, in Abaqus designated as *C3D8*-type elements, have been tested during the study. For this element type, the accuracy and the stability of the performed simulations were comparable to the reference Besseling model. Similarly, initial testing on parabolic three-dimensional structural finite elements, in Abaqus designated as *C3D20*-type elements, has also shown stable calculations using the presented method. However, further testing of

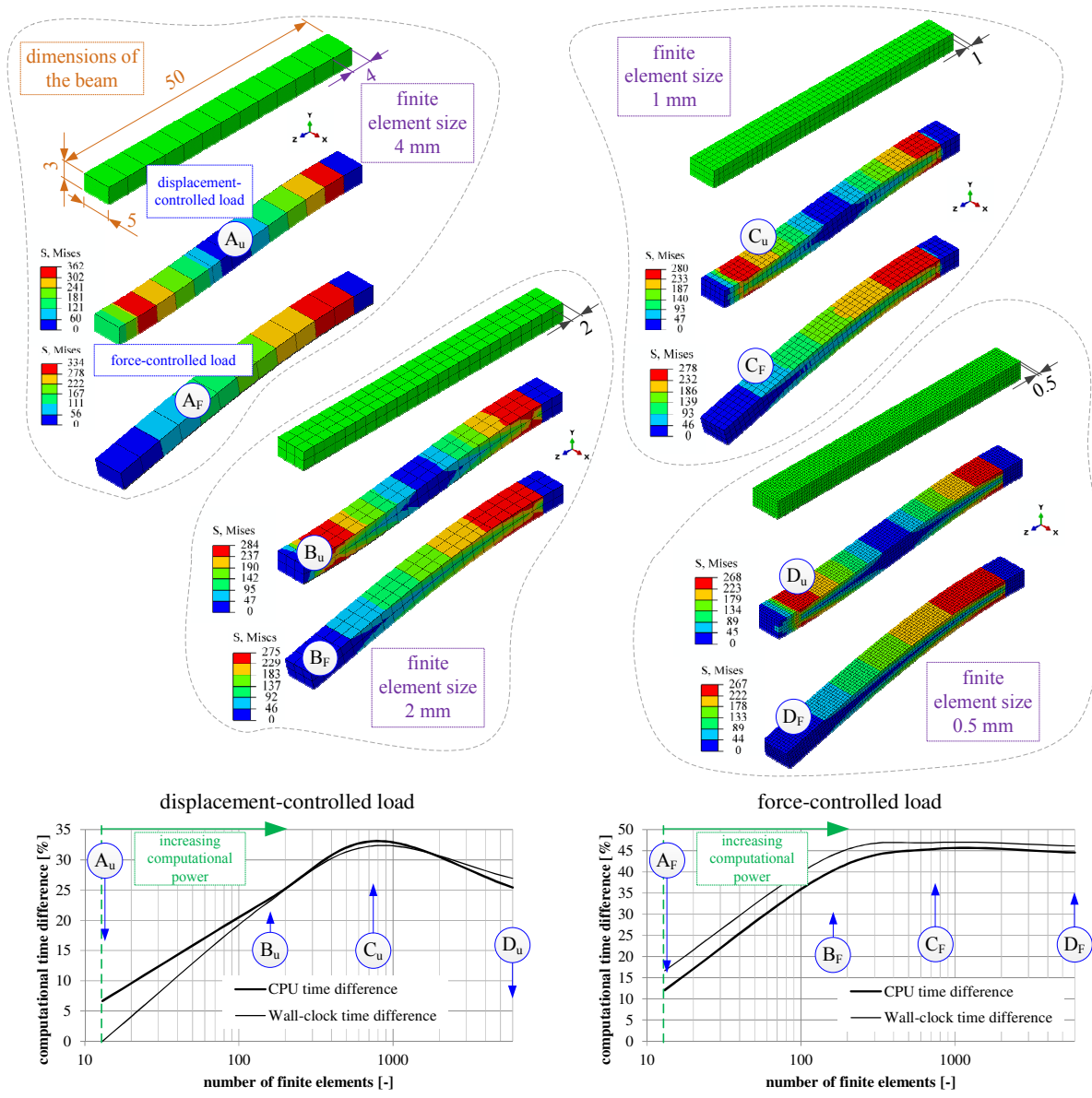


Figure 19: Comparison of computational times for various sizes of finite element meshes of both displacement-controlled and force-controlled cantilever beam. The deformed shapes, magnified by a factor of 10, are depicted after the first load step (10 s).

the method on parabolic structural finite elements is the case of the on-going research.

The presented procedure using the Prandtl operator approach in finite element analyses has so far provided very promising results for simulations of elastoplastic mechanical components subjected to variable thermomechanical loadings. Both the use of piecewise constant

hardening parameters between the yield functions and the simulation of their movement during the loading enable avoiding iterations in the stress-tensor increment calculation. Accompanied by the calculation of the Prandtl densities, performed prior to the simulation, the Prandtl operator approach results in shorter computational times as the reference model. Although the performance of the Prandtl operator approach has been demonstrated on the presented examples, further validation on other benchmark examples, such as a perforated plate or similar, will need to be undertaken. The model in the present form considers circular yield functions in the deviatoric plane and follows their movement in the radial direction. However, a separate consideration of the back-strains in both the normal and the shear directions and the introduction of non-circular yield functions will enable stress-strain simulations of more complex material behaviour. Future work will therefore concentrate on improvements to the model, considering a two-dimensional back-strain description and other shapes of yield functions that will extend its applicability to solids demonstrating anisotropic and asymmetric stress-strain behaviour. Currently, the approach enables consideration of the multilinear kinematic hardening. The inclusion of the isotropic hardening is already in progress, whereas the mixed hardening laws are planned for the future research. Furthermore, future studies will also examine an extension of the model to include the effects of viscoplastic material properties, which has proven to be a reasonable next step in our previous non-FE simulations. Last but not least, we see great potential for the model in the availability of the scalar values $\Delta\rho_s$ and $\Delta\rho_e$ in the very core of the method, which enable a straightforward implementation of both our previously developed methods for dissipated energy and fatigue or creep damage simulations and these methods developed by other researchers.

4. Conclusions

The paper has investigated a closed-form solution of elastoplastic stress-strain response modelling using the Prandtl operator approach. The approach proves to be appropriate for simulating the temperature-dependent, stress-strain behaviour of solids during loading. Furthermore, a comparison with the Besseling model reveals barely distinguishable results

during variable loading at constant temperature and slight discrepancies with a variable temperature. The comparison of the computational times showed up to 45 % shorter simulations using the Prandtl operator approach.

Acknowledgement

The authors acknowledge financial support from the Slovenian Research Agency (research core funding No. P2-0182 entitled Development Evaluation).

References

- [1] A. Yoosefian, M. Golmakani, M. Sadeghian, Nonlinear bending of functionally graded sandwich plates under mechanical and thermal load, *Communications in Nonlinear Science and Numerical Simulation* 84 (2020) 105161.
- [2] G. Liu, S. Winwood, K. Rhodes, S. Biroasca, The effects of grain size, dendritic structure and crystallographic orientation on fatigue crack propagation in in713c nickel-based superalloy, *International Journal of Plasticity* 125 (2020) 150 – 168.
- [3] Q.-L. Zhang, L. Hu, C. Hu, H.-G. Wu, Low-cycle fatigue issue of steel spiral cases in pumped-storage power plants under china’s and us’s design philosophies: A comparative numerical case study, *International Journal of Pressure Vessels and Piping* 172 (2019) 134 – 144.
- [4] L. Zhao, L. Xu, Y. Han, H. Jing, Z. Gao, Modelling creep-fatigue behaviours using a modified combined kinematic and isotropic hardening model considering the damage accumulation, *International Journal of Mechanical Sciences* 161-162 (2019) 105016.
- [5] M. Khazaei, S. Khadem, A. Moslemi, A. Abdollahi, Vibration mitigation of a pipe conveying fluid with a passive geometrically nonlinear absorber: a tuning optimal design, *Communications in Nonlinear Science and Numerical Simulation* 91 (2020) 105439.
- [6] D. Šeruga, E. Hansenne, V. Haesen, M. Nagode, Durability prediction of en 1.4512 exhaust mufflers under thermomechanical loading, *International Journal of Mechanical Sciences* 84 (2014) 199 – 207.
- [7] M. Callaghan, S. Humphries, M. Law, M. Ho, K. Yan, W. Yeung, Specimen-size dependency and modelling of energy evolution during high-temperature low-cycle fatigue of pressure vessel steel, *Scripta Materialia* 65 (4) (2011) 308 – 311.
- [8] R. Pandey, K. Shukla, A. Jain, Thermoelastic stability analysis of laminated composite plates: An analytical approach, *Communications in Nonlinear Science and Numerical Simulation* 14 (4) (2009) 1679 – 1699.

- [9] X. fang Xie, W. Jiang, J. Chen, X. Zhang, S.-T. Tu, Cyclic hardening/softening behavior of 316l stainless steel at elevated temperature including strain-rate and strain-range dependence: Experimental and damage-coupled constitutive modeling, *International Journal of Plasticity* 114 (2019) 196 – 214.
- [10] J. Li, I. Romero, J. Segurado, Development of a thermo-mechanically coupled crystal plasticity modeling framework: Application to polycrystalline homogenization, *International Journal of Plasticity* 119 (2019) 313 – 330.
- [11] D. Šeruga, M. Nagode, A new approach to finite element modelling of cyclic thermomechanical stress-strain responses, *International Journal of Mechanical Sciences* 164 (2019) 105139.
- [12] T. Brepols, S. Wulfinghoff, S. Reese, A gradient-extended two-surface damage-plasticity model for large deformations, *International Journal of Plasticity* 129 (2020) 102635.
- [13] O. F. Yilmaz, G. Ozcelik, F. B. Yeni, Lean holistic fuzzy methodology employing cross-functional worker teams for new product development projects: A real case study from high-tech industry, *European Journal of Operational Research* 282 (3) (2020) 989 – 1010.
- [14] P. Afonso, M. Nunes, A. Paisana, A. Braga, The influence of time-to-market and target costing in the new product development success, *International Journal of Production Economics* 115 (2) (2008) 559 – 568, institutional Perspectives on Supply Chain Management.
- [15] N. Ottosen, M. Ristinmaa, *The Mechanics of Constitutive Modeling*, Elsevier Science, 2005.
- [16] W.-F. Chen, D.-J. Han, *Plasticity for Structural Engineers*, J. Ross Publishing, 2007.
- [17] W. Lode, Versuche ber den Einflu der mittleren Hauptspannung auf das Flieen der Metalle Eisen, Kupfer und Nickel, *Zeitschrift fr Physik* 36 (11) (1926) 913–939.
- [18] B. Paliwal, Y. Hammi, M. Chandler, R. Moser, M. Horstemeyer, A three-invariant cap-viscoplastic rate-dependent-damage model for cementitious materials with return mapping integration in haigh-westergaard coordinate space, *International Journal of Solids and Structures* 182-183 (2020) 77 – 99.
- [19] A. Piccolroaz, D. Bigoni, Yield criteria for quasibrittle and frictional materials: A generalization to surfaces with corners, *International Journal of Solids and Structures* 46 (20) (2009) 3587 – 3596.
- [20] D. Zarkovic, D. Jovanovic, V. Vukobratovic, Z. Brujic, Convergence improvement in computation of strain-softening solids by the arc-length method, *Finite Elements in Analysis and Design* 164 (2019) 55 – 68.
- [21] Y. Lee, J. Ghosh, The significance of j_3 to the prediction of shear bands, *International Journal of Plasticity* 12 (9) (1996) 1179 – 1197.
- [22] L. Driemeier, S. P. Baroncini Proenca, M. Alves, A contribution to the numerical nonlinear analysis of three-dimensional truss systems considering large strains, damage and plasticity, *Communications in Nonlinear Science and Numerical Simulation* 10 (5) (2005) 515 – 535.
- [23] R. Hill, *The Mathematical Theory of Plasticity*, Oxford University Press, 1950.

- [24] E. Melan, Zur plastizität des räumlichen kontinuums, *Ing. Arch.* 9 (1938) 116–126.
- [25] D. W. Prager, The theory of plasticity: A survey of recent achievements, *Proceedings of the Institution of Mechanical Engineers* 169 (1) (1955) 41–57.
- [26] J. Lee, H. J. Bong, S.-J. Kim, M.-G. Lee, D. Kim, An enhanced distortional-hardening-based constitutive model for hexagonal close-packed metals: Application to az31b magnesium alloy sheets at elevated temperatures, *International Journal of Plasticity* 126 (2020) 102618.
- [27] Z. Qi, N. Hu, G. Li, D. Zeng, X. Su, Constitutive modeling for the elastic-viscoplastic behavior of high density polyethylene under cyclic loading, *International Journal of Plasticity* 113 (2019) 125 – 144.
- [28] R. Xing, D. Yu, S. Shi, X. Chen, Cyclic deformation of 316l stainless steel and constitutive modeling under non-proportional variable loading path, *International Journal of Plasticity* 120 (2019) 127 – 146.
- [29] C. Luo, W. Zeng, J. Sun, H. Yuan, Plasticity modeling for a metastable austenitic stainless steel with strain-induced martensitic transformation under cyclic loading conditions, *Materials Science and Engineering: A* 775 (2020) 138961.
- [30] C. Madrigal, A. Navarro, V. Chaves, A simplified plasticity model for multiaxial non-proportional cyclic loading, *Theoretical and Applied Fracture Mechanics* 103 (2019) 102247.
- [31] M. P. Petkov, J. Hu, E. Tarleton, A. C. Cocks, Comparison of self-consistent and crystal plasticity fe approaches for modelling the high-temperature deformation of 316h austenitic stainless steel, *International Journal of Solids and Structures* 171 (2019) 54 – 80.
- [32] E. A. E. Rodas], R. W. Neu, Crystal viscoplasticity model for the creep-fatigue interactions in single-crystal ni-base superalloy cmsx-8, *International Journal of Plasticity* 100 (2018) 14 – 33.
- [33] A. Cruzado, S. Lucarini, J. LLorca, J. Segurado, Microstructure-based fatigue life model of metallic alloys with bilinear coffin-manson behavior, *International Journal of Fatigue* 107 (2018) 40 – 48.
- [34] H. Farooq, G. Cailletaud, S. Forest, D. Ryckelynck, Crystal plasticity modeling of the cyclic behavior of polycrystalline aggregates under non-symmetric uniaxial loading: Global and local analyses, *International Journal of Plasticity* 126 (2020) 102619.
- [35] E. Haibach, *Betriebsfestigkeit - Verfahren und Daten zur Bauteilberechnung*, Springer-Verlag Berlin Heidelberg, 2006.
- [36] V. Okorokov, Y. Gorash, D. Mackenzie, R. van Rijswijk, New formulation of nonlinear kinematic hardening model, part ii: Cyclic hardening/softening and ratcheting, *International Journal of Plasticity* 122 (2019) 244 – 267.
- [37] S. Hartmann, W. Bier, High-order time integration applied to metal powder plasticity, *International Journal of Plasticity* 24 (1) (2008) 17 – 54.
- [38] L. H. Nguyen, D. Schillinger, The multiscale finite element method for nonlinear continuum localization problems at full fine-scale fidelity, illustrated through phase-field fracture and plasticity, *Journal of*

- Computational Physics 396 (2019) 129 – 160.
- [39] I. GosciniaK, K. Gdawiec, Control of dynamics of the modified newton–raphson algorithm, *Communications in Nonlinear Science and Numerical Simulation* 67 (2019) 76 – 99.
 - [40] K. Krabbenhøft, Basic computational plasticity, Tech. rep., Technical University of Denmark, Copenhagen (2002).
 - [41] M. Nagode, F. Zingsheim, An online algorithm for temperature influenced fatigue life estimation: strain-life approach, *International Journal of Fatigue* 26 (2) (2004) 155 – 161.
 - [42] M. Nagode, M. Fajdiga, Temperature-stress-strain trajectory modeling during thermo-mechanical fatigue, *Fatigue Fract Engng Matr Struct* 29 (2005) 175–182.
 - [43] M. Nagode, M. Fajdiga, Thermo-Mechanical Modelling of Stochastic Stress-Strain States, *Journal of Mechanical Engineering* 52 (2006) 74–84.
 - [44] M. Nagode, M. Fajdiga, Coupled elastoplasticity and viscoplasticity under thermomechanical loading, *Fatigue & Fracture of Engineering Materials & Structures* 30 (6) (2007) 510–519.
 - [45] M. Nagode, M. Hack, M. Fajdiga, Low cycle thermo-mechanical fatigue: damage operator approach, *Fatigue Fract Engng Matr Struct* 33 (2009) 149–160.
 - [46] M. Nagode, F. Laengler, M. Hack, A time-dependent damage operator approach to thermo-mechanical fatigue of ni-resist d-5s, *International Journal of Fatigue* 33 (5) (2011) 692 – 699.
 - [47] U. Šolinc, J. Klemenc, M. Nagode, D. Šeruga, A direct approach to modelling the complex response of magnesium AZ31 alloy sheets to variable strain amplitude loading using Prandtl-Ishlinskii operators, *International Journal of Fatigue* 127 (2019) 291 – 304.
 - [48] M. Nagode, F. Laengler, M. Hack, Damage operator based lifetime calculation under thermo-mechanical fatigue for application on ni-resist d-5s turbine housing of turbocharger, *Engineering Failure Analysis* 18 (6) (2011) 1565 – 1575.
 - [49] M. Nagode, D. Šeruga, M. Hack, E. Hansenne, Damage operator-based lifetime calculation under thermomechanical fatigue and creep for application on uginox f12t en 1.4512 exhaust downpipes, *Strain* 48 (3) (2012) 198–207.
 - [50] M. Nagode, A. Gosar, M. Hack, E. Hansenne, D. Šeruga, A review of thermomechanical fatigue damage calculations with the damage operator approach, in: *LCF8 - Eighth International Conference on Low Cycle Fatigue*, 2016.
 - [51] B. Kozjek, D. Šeruga, T. Pepelnjak, M. Nagode, Fatigue life prediction of brass ball forging tool, *Materials Today: Proceedings* 4 (5, Part 1) (2017) 5855 – 5860, 33rd Danubia Adria Symposium on Advances in Experimental Mechanics, 20-23 September 2016.
 - [52] M. Bartošk, M. Španiel, K. Doubrava, Thermo-mechanical fatigue of simo 4.06 turbocharger turbine housing: Damage operator approach, *Engineering Failure Analysis* 105 (2019) 736 – 755.

- [53] J. Besseling, A theory of elastic, plastic and creep deformations of an initially isotropic material, *Journal of Applied Mechanics* 25 (1958) 529–536.
- [54] D. Šeruga, M. Nagode, Comparative analysis of optimisation methods for linking material parameters of exponential and power models: An application to cyclic stress-strain curves of ferritic stainless steel, *Proceedings of the Institution of Mechanical Engineers, Part L: Journal of Materials: Design and Applications* 233 (9) (2019) 1802–1813.
- [55] D. Šeruga, M. Nagode, J. Klemenc, Eliminating friction between flat specimens and an antibuckling support during cyclic tests using a simple sensor, *Measurement Science and Technology* 30 (9) (2019) 095102.
- [56] J. Simo, R. Taylor, Consistent tangent operators for rate-independent elastoplasticity, *Computer Methods in Applied Mechanics and Engineering* 48 (1) (1985) 101 – 118.